



Cascading rupture process of the 2021 Maduo, China earthquake revealed by the joint inversion of seismic and geodetic data

Ao Zheng^a, Xiangwei Yu^a, Jiaqi Qian^a, Xiaoge Liu^{c,*}, Wenbo Zhang^{a,*}, Xiaofei Chen^b, Wenbin Xu^c

^a College of Earth and Planetary Sciences, University of Chinese Academy of Sciences, Beijing, China

^b Department of Earth and Space Sciences, Southern University of Science and Technology, Shenzhen, China

^c School of Geosciences and Info-Physics, Central South University, Changsha, China

ARTICLE INFO

Keywords:

Source rupture process
Maduo earthquake
Joint inversion
Tibetan Plateau

ABSTRACT

The 2021 M_w 7.4 Maduo earthquake occurred in the north-central Bayan Har block, which has been the most seismically active block of the Tibetan Plateau during recent decades. The Maduo earthquake provides an opportunity to study the rupture kinematics and seismogenic environment associated with subsidiary faults inside the block. We investigate the source rupture process of the Maduo earthquake by combining the seismological analyses and the joint inversion of geodetic and seismic data. We find that the source rupture propagates bilaterally on a splay fault geometry consisting of two steeply dipping segments. The slip distribution is dominated by sinistral slips and contains several asperities. The maximum slip is approximately 4.2 m, and the rupture duration is about 40 s. The spatiotemporal evolution of Coulomb failure stress (CFS) changes on the fault demonstrates the interactions of stress triggering between multiple asperities, indicating the cascading rupture process of the Maduo earthquake. Moreover, this event produces significant CFS increases on the subsidiary faults of the Bayan Har block, among which the Maduo-Gande and Tibet Dagou-Changmahe faults receive the largest stress loading. The occurrences of the 1947 Dari and 2021 Maduo earthquakes suggest that the seismic hazard of the subsidiary faults should not be neglected. Because the CFS on the Tuosuo Lake and Maqin-Maqu segments of the East Kunlun fault is also increased, the enhanced seismic hazard deserves further attention. In addition, the slip distribution illustrates that the source rupture is mainly concentrated in the brittle upper crust. We propose that the Maduo earthquake arises from the continuous loading on the internal fault of the Bayan Har block caused by the collision between the Eurasian and Indian plates, and the eastward extrusion of the middle-to-lower crustal flow facilitates the occurrence of this event. These factors constitute the seismogenic environment of the Maduo earthquake.

1. Introduction

The Tibetan Plateau resulted from the continental collision between the Eurasian and Indian plates, which has accommodated at least 2000 km of convergence since the Cenozoic. The ongoing tectonic loading has led to the uplift of the Tibetan Plateau, which is accompanied by intense seismicity (Molnar and Tapponnier, 1975; Royden et al., 1997; Clark and Royden, 2000; Tapponnier et al., 2001). The large-scale strike-slip faults in the Tibetan Plateau divide it into a series of active blocks, among which the Bayan Har block has been the most seismically active one over the past decades. The boundaries of the Bayan Har block are defined by the East Kunlun fault to the north, the Longmen Shan thrust

belt to the southeast, and the Ganzi-Yushu-Xianshuihe fault system to the south. Several major earthquakes have occurred in the Bayan Har block since the beginning of this century, including the 2008 M_w 7.9 Wenchuan earthquake (Shen et al., 2009; Wang et al., 2011), 2010 M_w 6.9 Yushu earthquake (Zhang et al., 2010; Li et al., 2011b), 2013 M_w 6.6 Lushan earthquake (Jiang et al., 2014; Li et al., 2014), 2014 M_w 6.9 Yutian earthquake (Li et al., 2016; Li et al., 2020) and the 2017 M_w 6.5 Jiuzhaigou earthquake (Sun et al., 2018; Zheng et al., 2020). These earthquakes are located near the margins of the Bayan Har block, reflecting that the tectonic strain is mainly concentrated on the block-bounding faults and thrusts. Hence the Bayan Har block was characterized by seismically active boundaries and the relatively rigid interior,

* Corresponding authors.

E-mail addresses: xiaogeliu@csu.edu.cn (X. Liu), wenbo@ucas.ac.cn (W. Zhang).

which moves eastward driven by tectonic loading (Tapponnier and Molnar, 1977; Tapponnier et al., 1982; Ren et al., 2022). However, this viewpoint is not consistent with the fact that the shear strain in some regions within the block were obviously observed and are not negligible compared to that of the block margins (Wang and Shen, 2020). Large earthquakes that occurred within the Bayan Har block are relatively rare, but numerous subsidiary faults that are subparallel to the East Kunlun and Ganzi-Yushu-Xianshuihe faults are developed in the block. The 1947 $M 7.7$ Dari earthquake ruptured the Dari fault inside the block (Molnar and Denq, 1984), suggesting that the tectonic strain accumulated on the subsidiary fault is capable of producing large earthquakes, but modern geophysical or geodetic observations are lacking for this event.

At 18:04:13 on 21 May 2021 (UTC), a $M_w 7.4$ earthquake, which is located approximately 70 km south to the East Kunlun fault, struck Maduo County in Qinghai Province, China. The epicenter of this event determined by the China Earthquake Networks Center (CENC) is at 34.59°N , 98.34°E , with a focal depth of 17 km. The 2021 Maduo earthquake is another large earthquake that occurred inside the Bayan Har block since the 1947 Dari earthquake, also representing the event with the largest magnitude since the destructive 2008 Wenchuan earthquake in China. The Maduo earthquake caused surface ruptures that were discovered in field investigations (Pan et al., 2021; Yuan et al., 2022). The surface ruptures were also recorded by the line-of-sight (LOS) displacements and pixel offsets derived from high-quality synthetic aperture radar (SAR) images (Zhao et al., 2021a; Liu et al., 2022). And the early aftershocks relocated by Wang et al. (2021b) indicated this event ruptured with a spatial extension of about 170 km. The western part of the surface rupture zone occurred along the preexisting Jiangcuo fault within the Bayan Har block (Wang et al., 2021b), whereas the eastern portion was probably along a previously unmapped fault (Ren et al., 2022). Apart from the geodetic observations like SAR interferograms (InSAR) or global positioning system (GPS) displacements, the seismic observations, including the strong-motion and teleseismic waveforms associated with the event, were also released and made available after the Maduo earthquake. The combination of multiple types of observations will supply an effectively spatiotemporal resolution for imaging the rupture process, and also help to overcome this limitation of the extractable information contained in a single type of data (Melgar and Bock, 2015). Therefore, the occurrence of the 2021 Maduo earthquake and the consummate multi-method observations provide us with a scarce opportunity to investigate the rupture kinematics of an earthquake inside the Bayan Har block and the seismogenic environment related to regional tectonics.

In this study, we reconstruct the source rupture process of the 2021 Maduo earthquake by combining the seismological analyses and the finite-fault joint inversion of seismic and geodetic data. We calculate the spatiotemporal evolution of CFS changes on the seismogenic fault. The regional seismic hazard is also evaluated based on the static CFS changes of surrounding active faults. We discuss the relationship between the focal mechanism and regional tectonics, and gain insights into the seismogenic environment of the Maduo earthquake and tectonic implications for the Bayan Har block.

2. Seismological analyses

2.1. W-phase moment tensor inversion

The moment tensor solution of the 2021 Maduo earthquake has been determined by several institutions, for example, the Global Centroid Moment Tensor (GCMT), the U.S. Geological Survey-National Earthquake Information Center (USGS-NEIC), and the CENC. Whereas the differences between these solutions blur the definiteness of the fault orientation of the Maduo earthquake (Table S1), we conduct the *W*-phase centroid moment tensor (WCMT) inversion (Kanamori and Rivera, 2008) independently to retrieve the focal mechanism solution.

Unlike the moment tensor inversion of the GCMT, which utilizes both body and surface waves (Ekstrom et al., 2012), the *W*-phase used in our inversion is the summation of multi-order normal modes (Kanamori and Rivera, 2008), which can ensure the rapid and stable inversion of moment tensor solution. 168 broadband waveforms collected from 73 global stations are used, and all traces are filtered in the passband between 0.002 and 0.006 Hz (Fig. S1), which is slightly modified from the frequency band adopted in the operation of the USGS-NEIC (Hayes et al., 2009; Duputel et al., 2012). The solution found after a grid search over focal depth and centroid location is shown in Fig. 1. The scalar moment is 1.54×10^{20} Nm ($M_w 7.39$), with the best double-couple nodal planes having strike, $\phi_1 = 282.0^\circ$, dip, $\delta_1 = 83.9^\circ$, and rake, $\lambda_1 = -8.6^\circ$, and $\phi_2 = 12.9^\circ$, $\delta_2 = 81.4^\circ$, and $\lambda_2 = -173.8^\circ$, for a focal depth of 15.5 km. The solution has a centroid time shift of 18.0 s and a centroid location at 34.650°N , 98.582°E , which is dependent on the PREM velocity model (Dziewonski and Anderson, 1981). Among the moment tensor solutions listed in Table S1, the WCMT solution is closer to the GCMT solution, which has a scalar moment of 1.71×10^{20} Nm ($M_w 7.42$), at a focal depth of 12.0 km. The WCMT solution suggests that the 2021 Maduo earthquake occurred on a steeply-dipping seismogenic fault, and the NE-dipping one of the two nodal planes is more consistent with the observed surface ruptures (Pan et al., 2021; Yuan et al., 2022) and the distribution of relocated aftershocks (Wang et al., 2021b).

2.2. Backprojection imaging

The backprojection approach is often implemented to reveal the spatiotemporal migration of high-frequency radiators of large earthquakes, which can help to constrain the fault rupture velocity, extent and duration (Ishii et al., 2005; Kruger and Ohrnberger, 2005; Yao et al., 2012; Kiser and Ishii, 2017). To achieve a high-resolution rupture imaging, we apply the Multiple Signal Classification (MUSIC) array processing technique, which can resolve closer simultaneous sources than conventional backprojection approaches (Meng et al., 2011; Bao et al., 2019). We backproject 385 teleseismic *P*-wave traces recorded by 368 broadband stations of the European network (Fig. S2) to image the high-frequency radiators of the 2021 Maduo earthquake. Before conducting the backprojection, the waveforms are bandpass-filtered between 0.5 and 2.0 Hz and aligned with respect to a reference trace by cross-correlation, and then traces with a signal-to-noise ratio (SNR) below 10 dB and cross-correlation coefficient with the reference trace below 0.5 are discarded. The waveforms aligned to the first *P*-wave arrival time are shown in Fig. S2. Due to the poor resolution at depth derived from the backprojection imaging, the grid search of high-frequency radiators is conducted on a 2-D horizontal plane. The horizontal plane is placed at a depth of 10 km and centered at 34.598°N , 98.251°E , which is the epicenter of the 2021 Maduo earthquake determined by the USGS-NEIC. We grid this plane into 101×301 blocks and place them at every 0.01° of both longitude and latitude. Each second, for 50 s after the first *P* arrival time, 10 s long *P*-wave trains are stacked with the differential slowness expected for each potential subevent on the gridded horizontal plane. This procedure detects coherent bursts of energy to determine the most likely location of rupture energy release.

The location of the local maximum in each time-window delineates the spatiotemporal evolution of high-frequency radiators (Fig. 1). The backprojection results suggest a bilateral rupture, and the energy release process can be divided into three stages. In the first stage (0–8 s), the rupture propagates at a relatively low velocity of about 1 km/s. The rupture seems to take place near the hypocenter, but the energy releasing rate is increasing constantly during the first stage (Fig. S2). The rupture propagation starts to speed up in the second stage (9–18 s), during which the rupture velocity once reaches about 3 km/s. While the energy releasing rate is dropping down rapidly during this stage. In the first two stages, the rupture extends predominately toward the northwest away from the initial point approximately 40 km. In the third stage (19 s later), the rupture turns to propagate at a steady velocity toward

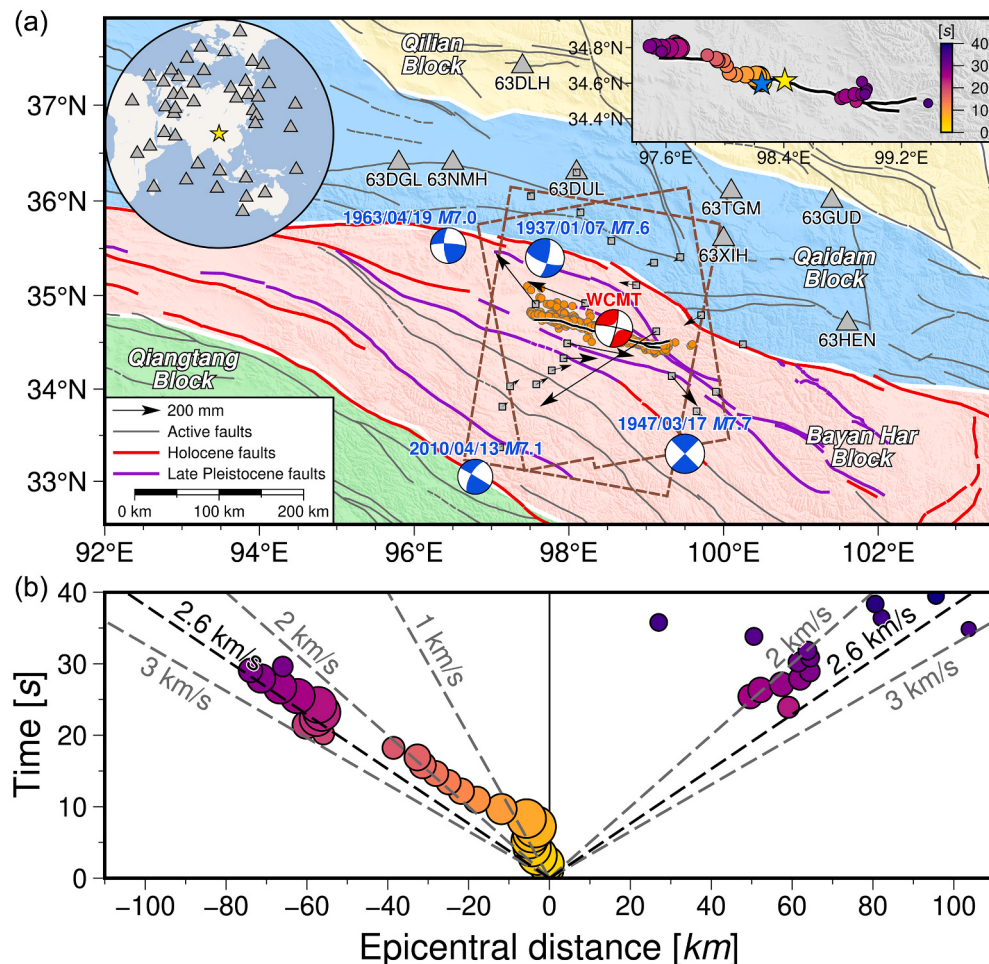


Fig. 1. (a) Map showing the study area for the 2021 M_w 7.4 Maduo earthquake. Tectonic secondary blocks in the Tibetan Plateau, including the Qilian, Qaidam, Bayan Har, Qiangtang blocks are plotted as colored patches. The Holocene and Late Pleistocene faults are shown by red and purple curves, respectively. Other active faults are shown by gray curves. The black curves indicate the fault traces of the source model of the 2021 Maduo earthquake. Blue beach balls, collected from Molnar and Deng (1984) and the GCMT, represent the focal mechanism solutions of the historical $M \geq 7.0$ earthquakes within the Bayan Har block since 1900. The red beach ball represents the WCMT solution of the 2021 Maduo earthquake. The aftershocks that followed 8 days after the mainshock were relocated by Wang et al. (2021b) and are plotted in orange circles. The gray triangles and those in the upper-left inset separately indicate the strong-motion and teleseismic stations used in this study. The brown dashed frames depict the coverage of Sentinel-1 interferograms. The black arrows denote the horizontal ground displacements acquired by GPS stations. The colored circles in the upper-right inset show the backprojected high-frequency radiators with areas proportional to the normalized energy and colors representing the rupture times, and the blue and yellow stars indicate the epicenter determined by the USGS-NEIC and the rupture starting point of the source model of the 2021 Maduo earthquake, respectively. (b) Distance of the backprojected high-frequency radiators away from the epicenter versus the rupture time. Westward and eastward ruptures are shown in the left and right panels, respectively. Reference rupture velocities are indicated by dashed lines. (For interpretation of the references to colour in this figure legend, the reader is referred to the web version of this article.)

both the northwest and southeast. The rupture duration indicated by the backprojection analysis is approximately 40 s. During the entire process, the rupture propagates toward the northwest and southeast about 80 and 100 km away from the rupture starting point, respectively. Additionally, the backprojected high-frequency radiators appear to be separated into three predominant clusters in space (Fig. 1). The occurrence of this phenomenon implies that multiple asperities may exist in the source rupture of the 2021 Maduo earthquake.

3. Finite-fault inversion

3.1. Geodetic data processing

The Sentinel-1 interferograms acquired in the ascending track 99 (Fig. 2a and b) and the descending track 106 (Fig. 2d and e) are used to retrieve the LOS displacements covering the epicentral area (Table S2). Following the standard two-pass InSAR data processing method (Xu et al., 2016), we process the interferograms using the GAMMA software (Wegmüller et al., 2016). The 30 m Shuttle Radar Topography Mission digital elevation model (SRTM DEM) is utilized to simulate and eliminate topographic signals (Farr et al., 2007). The interferograms are then filtered by an improved Goldstein filter (Li et al., 2008) and unwrapped using the minimum cost flow method (Chen and Zebker, 2001). Finally,

the unwrapped interferograms are geocoded into the World Geodetic System 84 coordinate system. We check the phase unwrapping results, mask areas with low coherence involving undetected unwrapping errors and subsample the unwrapped LOS displacements using the quadtree method (Jónsson et al., 2002). The static displacements of 22 GPS stations collected from Wang et al. (2021a) are also included in the analysis. Since the WCMT solution shows that the Maduo earthquake is dominated by a strike-slip focal mechanism, only the horizontal components of the stations located within 200 km from the epicenter are adopted, and the vertical components are excluded due to larger uncertainties.

3.2. Seismic data processing

Owing to complicated geomorphologic conditions, strong-motion stations are not densely distributed in the vicinity of the epicenter. We use the three-component strong-motion acceleration waveforms at 8 stations of the China Strong Motion Network operated by the Institute of Engineering Mechanics, China Earthquake Administration (CEA). Their epicentral distances range from 190 to 330 km. The initial strong-motion data has been preprocessed, integrated into velocity waveforms, bandpass-filtered between 0.1 and 0.4 Hz, and resampled at 5 Hz. The strong-motion stations are indicated by the gray triangles with station

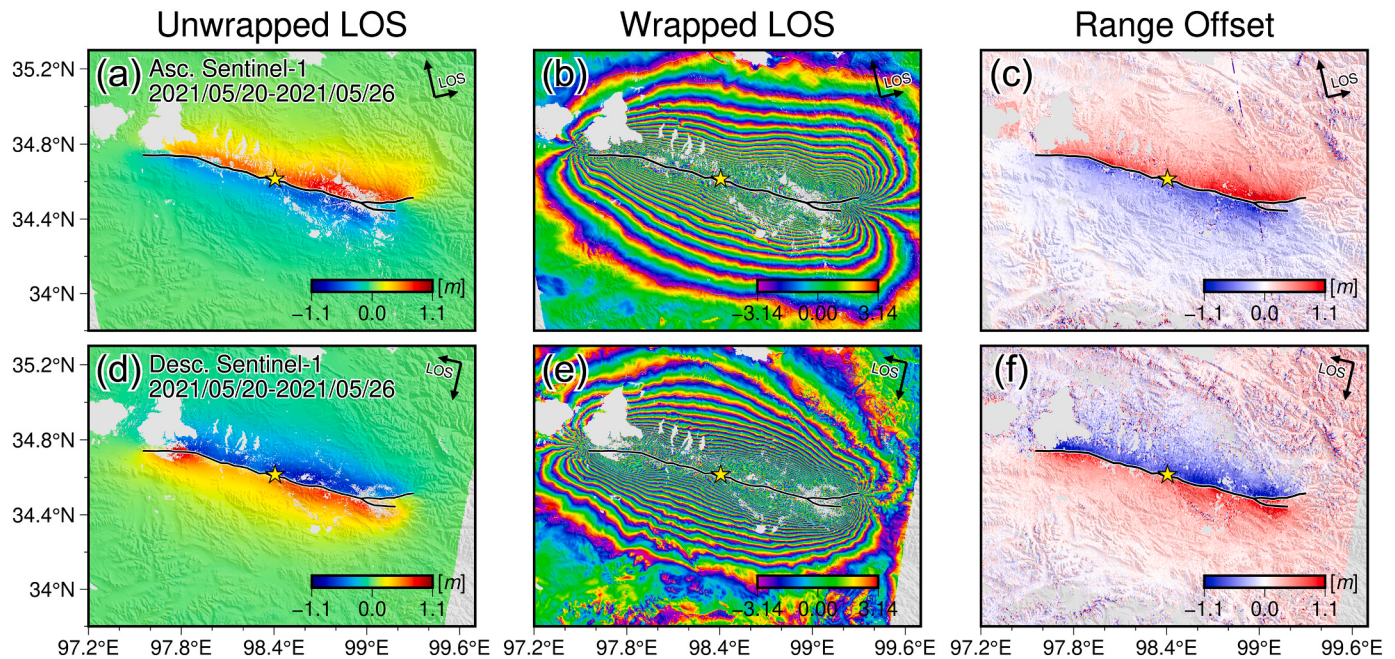


Fig. 2. (a, d) InSAR LOS unwrapped displacements, (b, e) wrapped interferograms, and (c, f) range pixel offsets of ascending and descending tracks observed between 20 May 2021 and 26 May 2021. The black curves indicate the fault traces of the source model of the 2021 Maduo earthquake, and the yellow star indicates the rupture starting point. (For interpretation of the references to colour in this figure legend, the reader is referred to the web version of this article.)

names in Fig. 1a. To improve the azimuthal coverage and expand the data types, 44 *P* and 40 *SH* teleseismic waves at epicentral distances ranging between 30° and 90° (Fig. 1a) collected from the Data Management Center of the Incorporated Research Institutions for Seismology (IRIS DMC) are also included. The instrument response is removed from the initial records to produce displacement waveforms (Wald et al., 1996), and then the waveforms are bandpass-filtered between 0.005 and 0.5 Hz and resampled at 5 Hz.

3.3. Joint inversion strategy

In the ascending and descending LOS displacement fields (Fig. 2a and d), it is clear that the displacements at opposite directions are separated by a roughly NW-SE trending fault trace. The deformation pattern in the range pixel offsets (Fig. 2c and f) collected from Liu et al. (2022), in which the E-W component of the complete 3-D displacement predominates, resembles that of the unwrapped LOS displacements. Moreover, it is easily definable in the range offsets that the fault trace splay into two strands at its eastern extremity. For a roughly NW-SE trending fault, the E-W displacement extends nearly throughout the entire rupture zone in both unwrapped LOS displacements and range offsets. The opposite motions on both sides of the fault are consistent with the sinistral-slip fault motion and the spatial distribution of aftershocks (Wang et al., 2021b). The WCMT solution also indicates that the Maduo earthquake occurred on a strike-slip fault with a non-double-couple component of approximately 20%, implying a certain complexity of the focal mechanism. Consequently, we build a branch fault geometry comprising two fault segments and determine the corresponding surface traces depending on the nearly E-W trending discontinuous boundary of the ground deformation acquired by geodetic observations (Fig. 2). The relocated aftershocks that distribute on both sides of the fault trace confuse the dipping direction of the causative fault (Fig. 1). Fixing the location of the surface traces, we perform static inversions of InSAR and GPS data to search the optimal dip angles for the two fault segments (Fig. S3 and S4). The along-dip width of each fault segment is set as 28 km and the two fault planes are then discretized into 4 km × 4 km subfaults.

We obtain the rupture kinematics of the two-segment fault model through the joint inversion of the LOS displacements of Sentinel-1 interferograms, static GPS displacements, teleseismic *P* and *SH* waves and three-component strong-motion waveforms. From the near-field to regional range of the source area, the velocity model is assumed as a horizontally layered structure (Shen et al., 2016) modified by the empirical relations of Brocher (2005). Based on the regional velocity model, the Green's functions of the strong-motion waveform, InSAR and GPS data are calculated using the frequency wavenumber integration code FK (Zhu and Rivera, 2002). Based on the CRUST1.0 model (Laske et al., 2013), the Green's functions of teleseismic *P* and *SH* waves are generated by Multitel3 developed by Qian et al. (2017). In accordance with the WCMT solution, the slip rake of subfaults is allowed within $-90^\circ \pm 45^\circ$. Our inversion exploit the linear multi-time-window method (Olson and Apsel, 1982; Hartzell and Heaton, 1983) to resolve the spatiotemporal rupture process, with further details available in Zheng et al. (2018). Due to the inevitable trade-off between the prescribed rupture velocity (the triggering velocity of the first time-window) and the rise time of time-window, a systematic grid search is implemented by performing a series of inversion trials. The variation of rupture velocity existing within the rupture process was proposed by previous studies (Lyu et al., 2022; Yue et al., 2022), thus the propagating velocity on both rupture directions in our inversion is allowed to be different to accommodate this possible flexibility. By evaluating the normalized misfit of all the observed data, we test the prescribed rupture velocities from 1.0 to 4.0 km/s with an interval of 0.2 km/s, and rise times of time-window from 0.8 to 3.6 s with an interval of 0.4 s. As shown in Fig. S5, the optimal result suggests that the westward and eastward ruptures both prefer an identical propagating velocity of 2.6 km/s, which is slightly higher than the average rupture velocity revealed by the backprojection analysis (Fig. 1). Fixing the rupture velocity as the preferred value, the misfit curve illustrates that the rise time of 2.4 s yields the best data fitting, which allows a maximum duration of 8.4 s within 6 half-overlapping triangle time-windows. All datasets are initially normalized by the corresponding Frobenius norms (Chen et al., 2018), and the preferred weighting scheme for the InSAR LOS displacements, static GPS displacements, strong-motion and teleseismic waveforms are 1.0, 0.3,

0.3 and 0.1, respectively. A revised Laplacian smoothing (Zheng et al., 2020) is introduced to stabilize the inversion. The hyper-parameter, the smoothing factor, is selected by evaluating the trade-off curve between the model roughness and the normalized misfit. As shown in Fig. S6, the smoothing factor is chosen as 0.0008 following the classic L-shaped curve.

4. Results

We test the dip angles of the two-segment fault model from SW-dipping 70° to NE-dipping 70° (equivalent to SW-dipping 110°), with an interval of 1°. Since the dip angle variation along the fault strike is slight (Hong et al., 2022), the two fault segments are assigned to the same dip. The trial and error of static inversions reveal that both fault segments dip northeastward steeply at 84° (Fig. S3), which is consistent with the WCMT solution in this study. The length of the main fault segment (#1) is 168 km, and the fault strike varies along the surface trace from west to east. On the westernmost side, the fault strike is close to purely EW until about 97.9°E. Subsequently, the main fault segment turns into WNW striking and extends eastward until the western extremity of the branch fault segment (#2). And the branch segment continues to extend 20 km eastward along a similar orientation. While on the easternmost side, the main segment rotates to WSW striking and

vanes at about 99.3°E. Hence, a two-segment fault model consisting of two curved fault planes is constructed to accommodate the variation of fault strike.

The best-fitting model of the joint inversion indicates that the slip distribution is dominated by sinistral slips (Fig. 3a), which confirms our aforementioned analysis based on the geodetic data. Major slips larger than 1 m are mainly concentrated at the depth of <20 km, and form several asperities. Furthermore, most of slips larger than 2 m are localized on the uppermost subfaults of both fault segments, suggesting that the stronger parts of the source rupture reach the ground surface and produce the observed surface ruptures associated with the 2021 Maduo earthquake. The peak slip of up to 4.2 m occurs adjacent to the branch of the two-segment fault model, where a set of high-frequency radiators determined by the backprojection analysis are also clustered, implying that the fault geometry probably controls the rupture pattern of this event (Lindh and Boore, 1981). The source rupture initiates near the center of the main fault segment, and expands updip and downdip around the rupture starting point as a circular-like crack rupture during the first 8 s. Most of subfaults start to rupture as soon as the first time-window is triggered (Fig. 3c and 4). Subsequently, the rupture front propagates bilaterally and lasts about 32 s. The slip rate functions of the subfaults with significant slips in several asperities also demonstrate that the source rupture evolves into two slip pulses propagating toward both

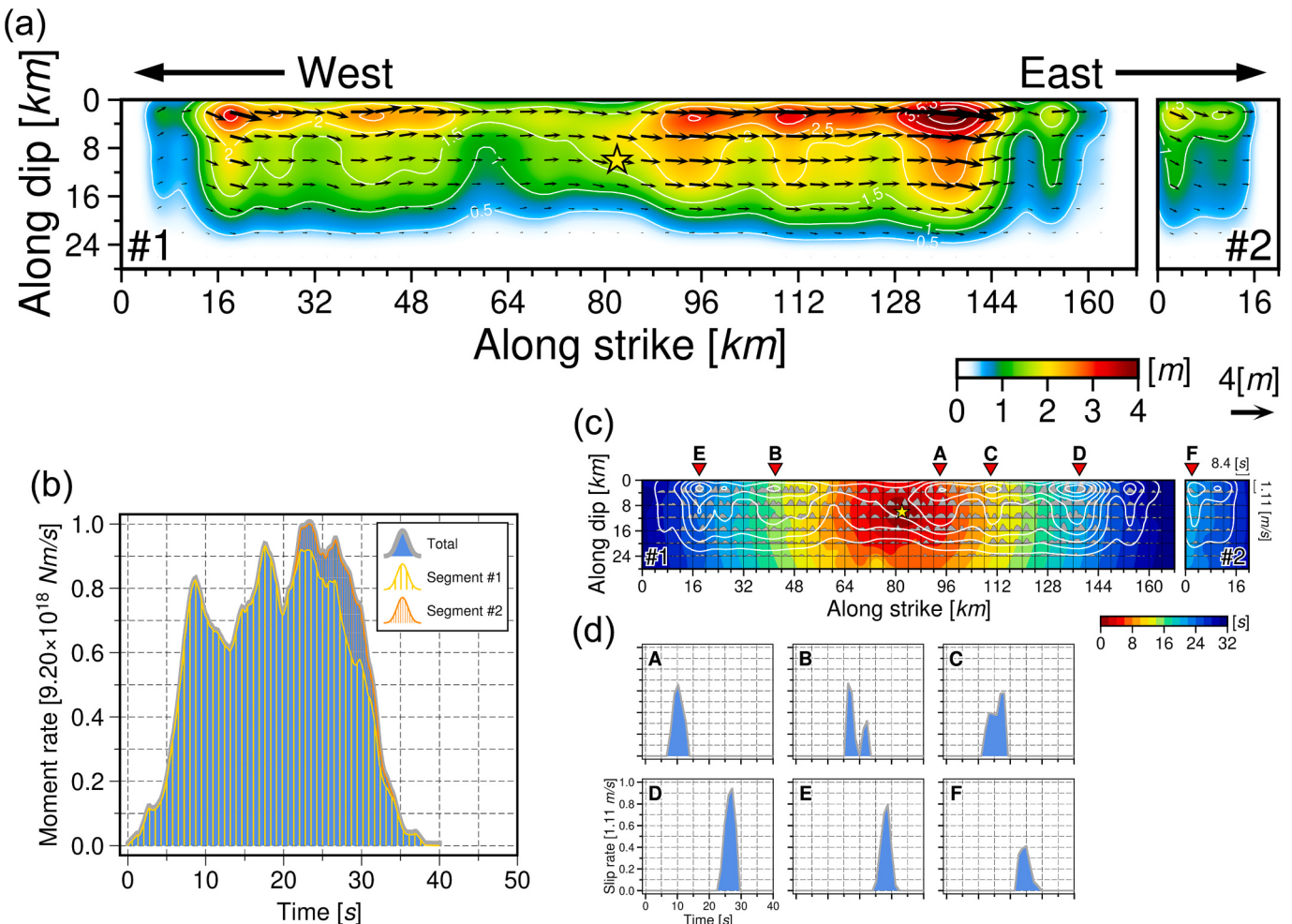


Fig. 3. (a) Slip distribution according to our preferred fault model derived from the joint inversion, in which #1 and #2 indicate the main and branch fault segments, respectively. The slip contour interval is 0.5 m, and the yellow star indicates the rupture starting point. (b) Total seismic moment releasing rate function of the branch fault model. The individual moment releasing rate functions of the main and branch fault segments are also separately plotted in yellow and orange lines. (c) Slip rate functions of the subfaults in the branch fault model, with the rupture front evolution with time as the background and the slip contours shown by white curves. (d) Slip rate functions of the uppermost subfaults on the fault plane shown in (c). (For interpretation of the references to colour in this figure legend, the reader is referred to the web version of this article.)

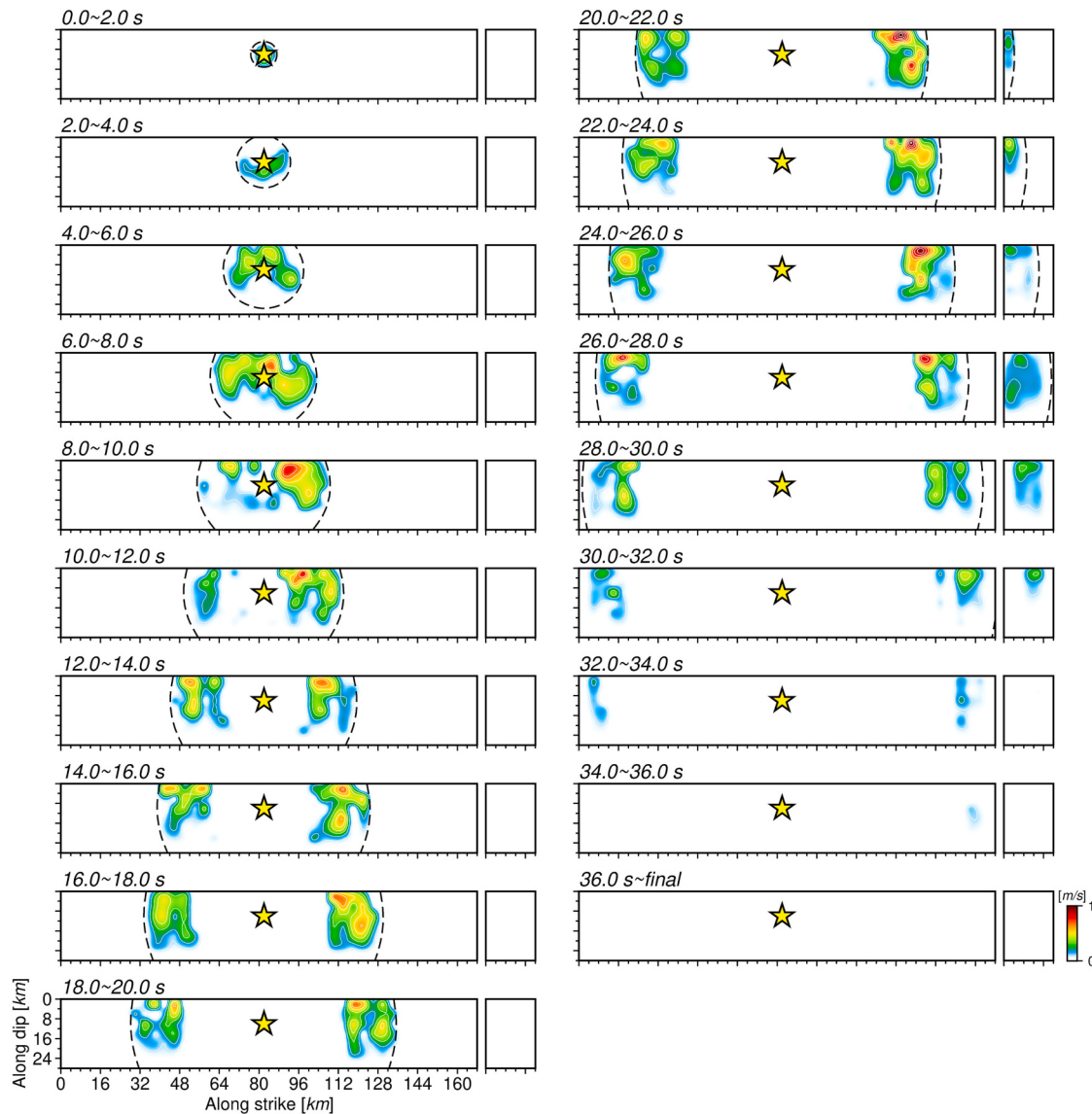


Fig. 4. Spatiotemporal evolution of the fault slip rate of the branch fault model derived from the joint inversion. The yellow star indicates the rupture starting point. The black dashed line represents the pseudo-rupture front with a bilateral rupture velocity of 2.6 km/s. (For interpretation of the references to colour in this figure legend, the reader is referred to the web version of this article.)

the northwest and southeast (Fig. 3d and 4). The rupture starts to migrates into the branch fault segment from 20 s after the rupture initiation and lasts approximately 14 s. Due to the contribution of the rupture of the branch segment, the moment releasing rate reaches a maximum of 9.20×10^{18} Nm/s at about 23 s (Fig. 4b). The entire rupture releases a scalar seismic moment of 1.75×10^{20} Nm (M_w 7.43), which is dominated by the seismic moment of 1.64×10^{20} Nm (M_w 7.41) released by the main fault segment, whereas the releasing moment of the branch segment is 1.11×10^{19} Nm (M_w 6.63). The examined geodetic and seismic data are well resolved by our preferred model (Figs. 5 and 6). The variance reductions (VRs) of the InSAR LOS data, static GPS displacements, strong-motion waveforms, and teleseismic P and SH waves are 97%, 99%, 65%, 66%, and 75%, respectively.

5. Discussion

5.1. Comparison of source rupture models

Several source rupture models of the 2021 Maduo earthquake have been obtained by utilizing different observed data and methods in

previous studies. The separate or joint inversion of geodetic observations, including static GPS displacements and SAR interferograms can be used to infer the fault slip distribution (Chen et al., 2021; He et al., 2021; Jin and Fialko, 2021; Wang et al., 2021a; Zhao et al., 2021a; Guo et al., 2022; He et al., 2022; Hong et al., 2022; Li et al., 2022; Tong et al., 2022; Wang et al., 2022). And the addition of seismic or high-rate GPS waveforms further enables the reconstruction of source rupture process (Chen et al., 2022; Lyu et al., 2022; Yue et al., 2022; Zhang et al., 2022b). To accommodate the complexity of fault geometry indicated by the surface ruptures and geodetic observations, some source models were constructed using curved faults (He et al., 2022; Hong et al., 2022; Wang et al., 2022; Yue et al., 2022) or composed of multiple planar faults with diverse orientations (He et al., 2021; Jin and Fialko, 2021; Zhao et al., 2021a; Chen et al., 2022; Zhang et al., 2022b). The easternmost branch fault is generally involved in the models of Chen et al. (2021), Chen et al. (2022), He et al. (2022), Hong et al. (2022), Jin and Fialko (2021), Wang et al. (2022), Zhao et al. (2021a) and our preferred model. Whereas the westernmost branch fault indicated by the relocated aftershocks (Wang et al., 2021b) only exists in the models of Guo et al. (2022) and He et al. (2021) due to lack of sufficient associated geodetic

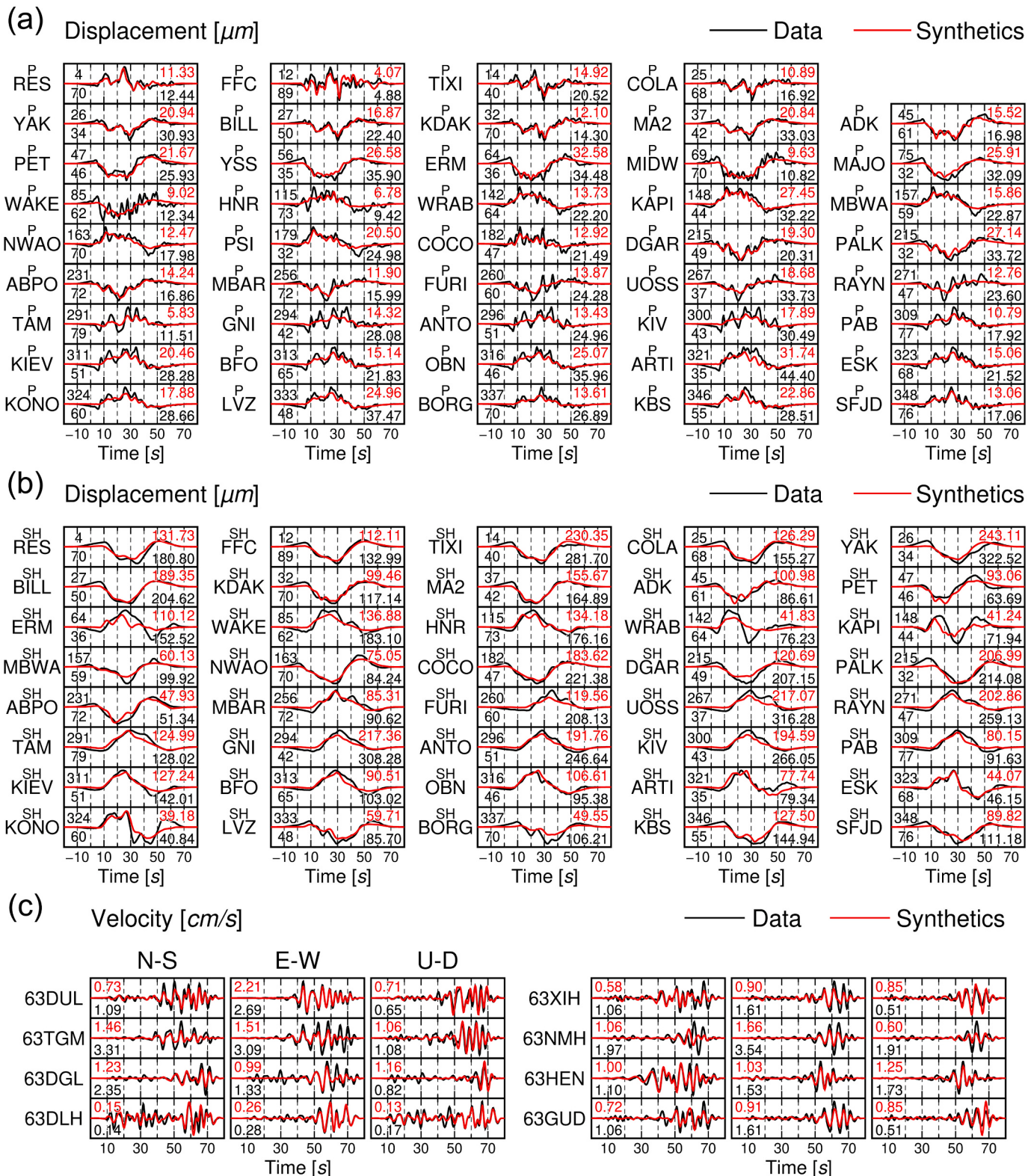


Fig. 5. (a, b) Comparison between the observed teleseismic (a) *P* waves and (b) *SH* waves (displacement) and the synthetic waveforms obtained from the joint inversion of the branch fault model. The maximum amplitudes of the observed (black font) and synthetic waveforms (red font) are shown to the right of each waveform, in micrometers. The azimuth and epicentral distance in degrees are shown at the beginning of each record with the azimuth on top. (c) Comparison between the observed strong-motion seismograms (velocity) and the synthetic waveforms obtained from the joint inversion of the branch fault model. The maximum amplitudes of the observed (black font) and synthetic waveforms (red font) are shown to the left of each waveform, in centimeters per second. (For interpretation of the references to colour in this figure legend, the reader is referred to the web version of this article.)

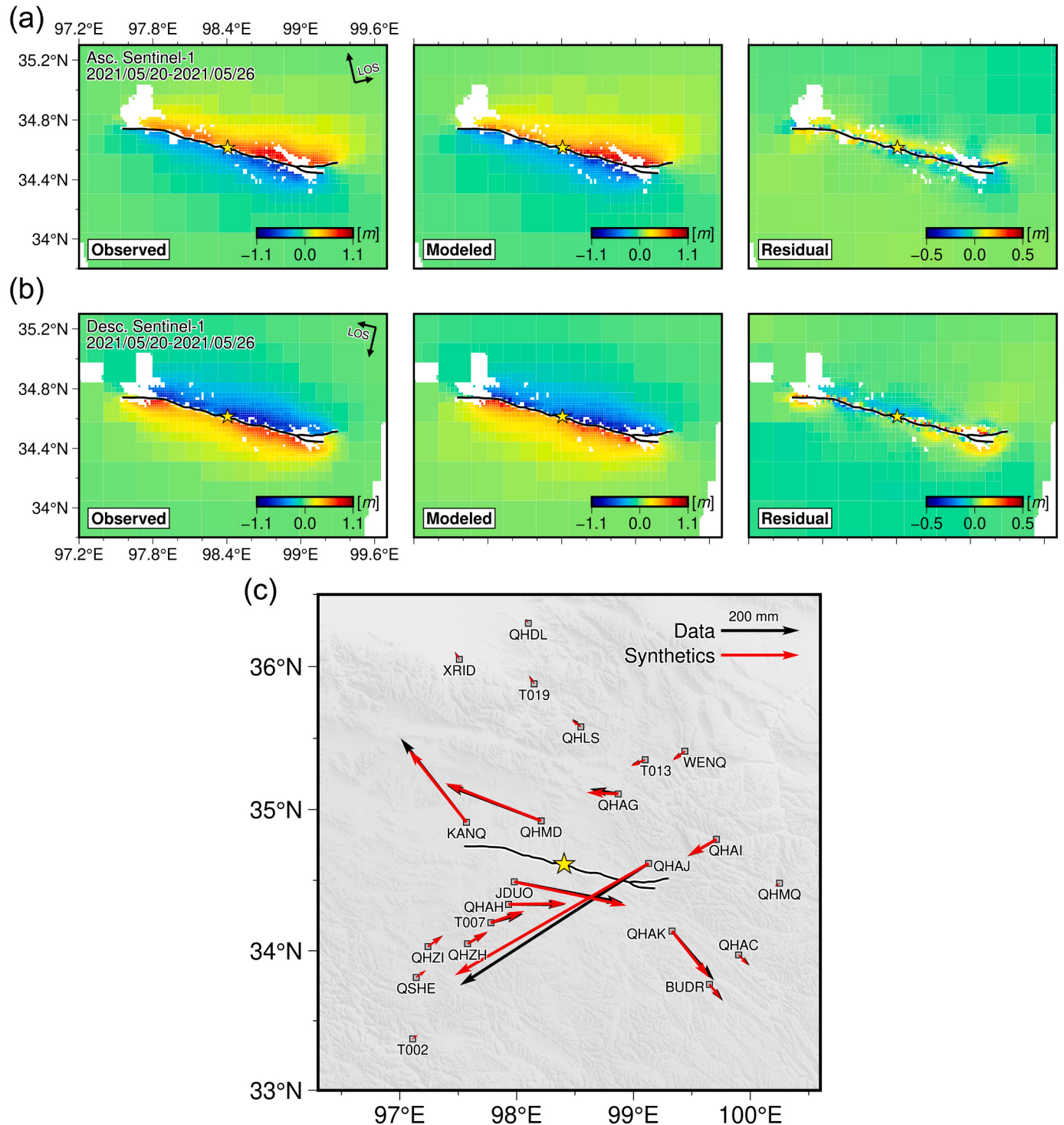


Fig. 6. (a, b) Unwrapped LOS displacements of the observed, modeled by the joint inversion of the branch fault model, and residual of the surface deformation field acquired by Sentinel-1 in (a) ascending track 99 and (b) descending track 106. (c) Comparison between the observed horizontal components of the static GPS displacements (black arrow) and the synthetic ones (red arrow) obtained from the joint inversion of the branch fault model. The black curves indicate the fault traces of the source model of the 2021 Maduo earthquake, and the yellow star indicates the rupture starting point. (For interpretation of the references to colour in this figure legend, the reader is referred to the web version of this article.)

observations. The previous inversions of rupture process and our preferred model all reveal the bilateral rupture of the Maduo earthquake. However, by means of the backprojection of high-frequency radiators, Li et al. (2022), Yue et al. (2022) and Zhang et al. (2022b) found that the propagating velocity of the eastward rupture is larger than that of the westward rupture and reaches a supershear rupture, which was

also proposed by Lyu et al. (2022) through the joint inversion including high-rate GPS waveforms. And Yue et al. (2022) and Zhang et al. (2022b) adopted a simpler fault geometry without the eastern branch fault. The backprojection analysis and the grid search of rupture velocity in this study attribute the Maduo earthquake to a subshear rupture probably reflecting the average of propagating velocity in the bilateral

rupture, which is closer to the model of Chen et al. (2022). Compared with the strong-motion stations used in this study, the GPS stations recording high-rate displacement waveforms are closer to the seismogenic fault and therefore more sensitive to the variation of rupture velocity during the rupture process (Lyu et al., 2022). The maximum slip of most models is approximately 4 to 6 m, but there are still some models with a maximum slip of >7 m (Guo et al., 2022; Tong et al., 2022). The slip distributions of these models are also different. There are at least three slip asperities in most models, also including our preferred model, but the model of Wang et al. (2021a) has only two asperities. In addition, significant slips are mainly concentrated near the fault top in the models of Hong et al. (2022), Yue et al. (2022) and this study. However, depending on the inversion using only InSAR data, Chen et al. (2021), Jin and Fialko (2021), Tong et al. (2022) and Zhao et al. (2021a) yielded the slight shallow slip deficit in the Maduo earthquake. Perhaps the subfault size of 4 km used in our study is not sufficiently fine to reflect the variation of fault slips at shallow depths, and the contribution from the InSAR data is weakened to some extent by the addition of other observed data in the joint inversion, hence there is no apparent shallow slip deficit in our preferred model. Based on the comparison of these models, it is difficult to directly distinguish which model is better, but it still helps to understand and evaluate the distinctive properties of the 2021 Maduo earthquake.

5.2. Coulomb failure stress evolution

It is still challenging to perceive the nature of source rupture due to the proposed viewpoints that have not been unified (Beroza and Ellsworth, 1996; Kato et al., 2012; Bouchon et al., 2013; Ellsworth and Bulut, 2018; Gomberg, 2018; Tape et al., 2018; Huang et al., 2020; Kato and Ben-Zion, 2021). The cascade model, in which the spontaneous rupture can sequentially trigger multiple asperities through stress transfer, is one of the end-member models for understanding the fault rupture (Ellsworth and Beroza, 1995; Marsan and Lengline, 2008; Ellsworth and Bulut, 2018). Our preferred model shows that the 2021 Maduo earthquake contains several asperities in the slip distribution. To understand whether the ruptures of multiple asperities are triggered by stress interaction, we analyze the spatiotemporal evolution of static CFS changes on the fault plane during the rupture process following the strategy of Zhang et al. (2020). The open software Coulomb3.3 developed by Toda et al. (2011) is used to calculate the CFS changes, with an effective friction coefficient of 0.4 (King et al., 1994). Due to the dominance of sinistral strike-slip component in the focal mechanism of the Maduo earthquake, the receiver fault is assumed as purely strike-slip in the calculation of CFS changes. As shown in Fig. 7, Asperity A is initiated at the onset of the source rupture, and the rupture in the first 3 s causes stress loading of 0.2 MPa in the area of Asperity A where

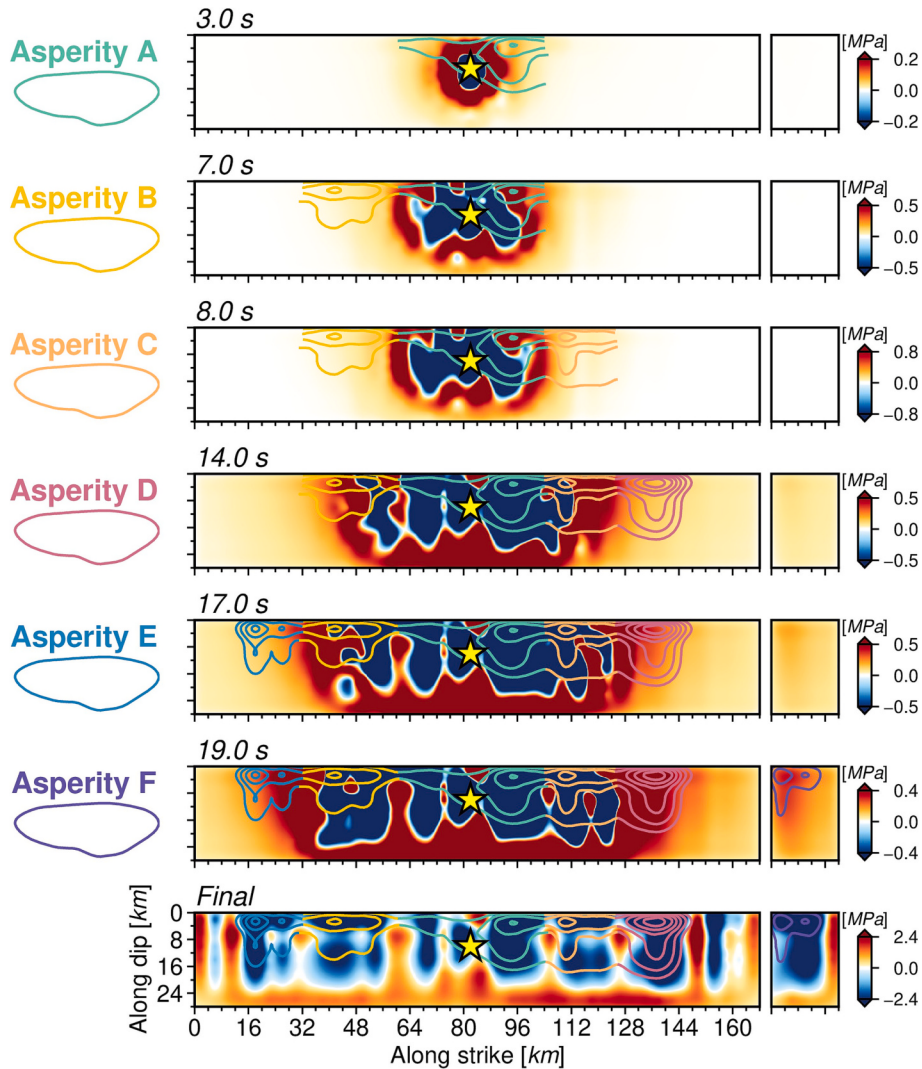


Fig. 7. Spatiotemporal CFS evolution on the fault plane of the 2021 Maduo earthquake. The yellow star indicates the rupture starting point. The slip contours are shown by colored curves with an interval of 0.5 m. (For interpretation of the references to colour in this figure legend, the reader is referred to the web version of this article.)

significant slips occur. And then, the CFS in Asperity B is increased up to 0.4 MPa by Asperity A at the rupture onset of Asperity B. Subsequently, the CFS changes near the western margin of Asperity C imparted by Asperity A and B are about 0.8 MPa. The rupture of Asperity D is initiated from its western margin where a CFS loading of approximately 0.4 MPa is induced by the first three asperities. Afterwards, the eastern margin of Asperity E is also loaded by the CFS changes of up to 0.7 MPa due to the contributions from the ruptures of previous asperities. In addition, the rupture of the main fault segment produces positive CFS changes on the branch fault segment, which reach 0.3 MPa at the rupture onset of Asperity F and further trigger its rupture. The CFS evolution indicates that the previously ruptured asperities always cause stress loading on the subsequent asperities, which has positive effects in triggering the successive ruptures of multiple asperities. Moreover, the CFS evolution on the fault shows that the CFS changes of the asperities remain negative after their ruptures, implying that the subsequent asperity is difficult to trigger the previous one to rupture again. Hence, we suggest that the rupture process of the 2021 Maduo earthquake can be attributed to the so-called cascade model.

5.3. Regional seismic hazard evaluation

The interaction between earthquakes is realized in a manner of earthquake triggering by the CFS changes, that is the positive CFS change brings the fault closer to failure, while the negative CFS change retards subsequent events (Stein, 1999, 2003; Freed, 2005). Based on the source rupture model derived from the joint inversion, we calculate the static CFS changes induced by the 2021 Maduo earthquake to illustrate the influences on the subsequent seismicity of surrounding active faults. The same strategy as that in the previous section is used, and the effective friction coefficient is assumed as a typical value of 0.4 (King et al., 1994). The geometry of receiver faults is adopted from Deng et al. (2003). As shown in Fig. 8, the 2021 Maduo earthquake produces significant CFS increases on the active faults on both the west and east of the seismogenic fault. The positive CFS changes on the western segment of the Gande Southern Margin fault and the middle segment of the Dari fault are up to 0.36 MPa and 0.10 MPa, respectively. Furthermore, the CFS increases on the middle segment of the Maduo-Gande fault and the eastern segment of the Tibet Dagou-Changmahe fault separately reach 4.50 MPa and 3.10 MPa. Even though the CFS disturbances do not

change the long-term accumulation of strain within the block, such substantial CFS increments may advance the occurrences of earthquakes. Evident CFS increases are also observed on the Bayan Har Main Peak and Wudaoliang-Changshagongma faults, both exceeding the earthquake triggering threshold 0.01 MPa (Hardebeck et al., 1998). The occurrences of the 1947 Dari and 2021 Maduo earthquakes, also including other smaller events, demonstrate that the tectonic strain is continuously accumulated inside the Bayan Har block, hence the seismic hazard of the internal faults of the block should not be neglected. The CFS on the segments of the East Kunlun fault is increased by the 2021 Maduo earthquake. The CFS increments on the Tuosuo Lake and Maqin-Maqu segments are 0.12 MPa and 0.01 MPa, respectively. The Tuosuo Lake segment is currently in a state of strong locking (Jian et al., 2022). The 1937 M 7.6 Huashixia earthquake has occurred on the Tuosuo Lake segment (Guo et al., 2007), indicating that this segment has the potential for a major earthquake. Moreover, the analysis of historical seismic catalogues revealed that the Maqin-Maqu segment has no records of $M_s \geq 6.5$ earthquakes for at least 300 years (Wen et al., 2007). The continuous strain increments on the Maqin-Maqu segment suggest it is probably in the later stage of earthquake cycle (Shan et al., 2015; Ou et al., 2022). Hence the seismic hazard on the Tuosuo Lake and Maqin-Maqu segments of the East Kunlun fault may be increased by the Maduo earthquake and deserves further attention.

5.4. Seismogenesis related to regional tectonics

Since previous large earthquakes mainly occurred along the boundary faults of the Bayan Har block, the strain associated with plate collision was naturally accumulated and released on these faults. Furthermore, the subsidiary faults inside the block receive less attention due to being seismically inactive. Inferred from GPS observations, the slip rate of the seismogenic fault hosting the 2021 Maduo earthquake is only 1.2 ± 0.8 mm/a (Zhu et al., 2021). However, the Bayan Har block is undergoing a high interseismic strain rate caused by the eastward extrusion of the Tibetan Plateau (Wang and Shen, 2020). And 10–40% of the strain is accumulated within the body of the Bayan Har block (Yue et al., 2022). The occurrence of the 2021 Maduo earthquake demonstrates that the subsidiary faults inside the block can also effectively accumulate strain and have the potential to further cause large earthquakes. But owing to the low slip rate, the recurrence period of an event

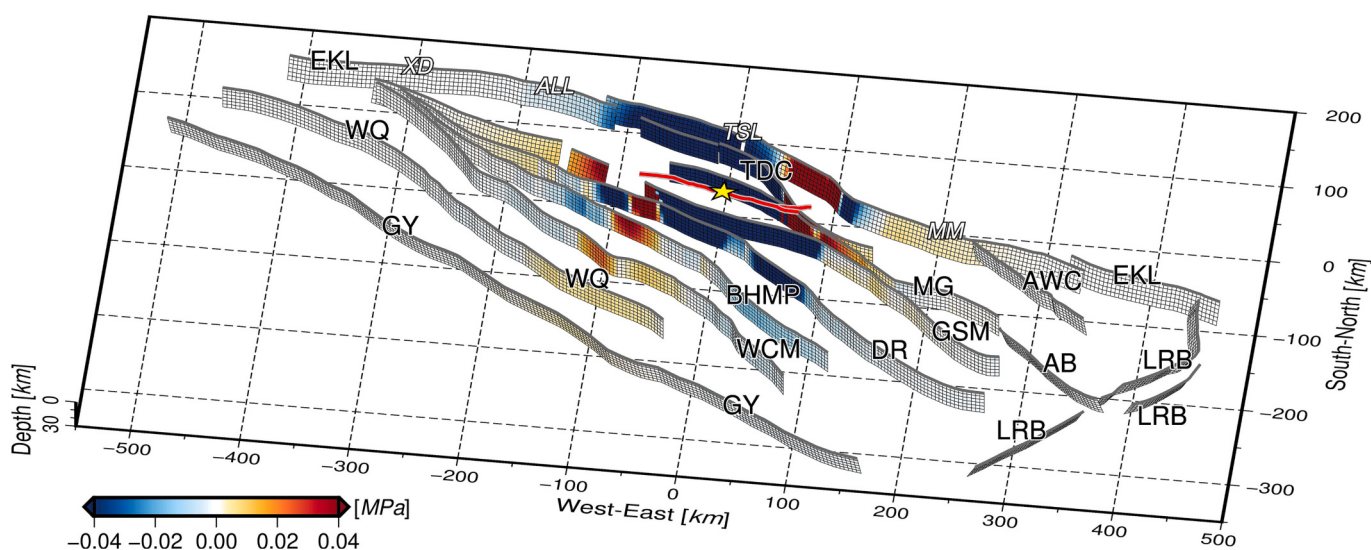


Fig. 8. Distribution of the static CFS changes on surrounding active faults induced by the 2021 Maduo earthquake. The fault abbreviations in black font are EKL = East Kunlun fault, TDC = Tibet Dagou-Changmahe fault, AWC = Awancang fault, MG = Maduo-Gande fault, GSM = Gande Southern Margin fault, BHMP = Bayan Har Mountain Peak fault, DR = Dari fault, AB = Aba fault, LRB = Longriba fault, WCM = Wudaoliang-Changshagongma fault, WQ = Wudaoliang-Qumalai fault, GY = Ganzi-Yushu fault. The abbreviations in white italic font represent the fault segments of the East Kunlun fault, including XD = Xidatan-Dongdatan segment, ALL = Alake Lake segment, TSL = Tuosuo Lake segment, MM = Maqin-Maqu segment.

analogous to the Maduo earthquake is about thousands of years (Guo et al., 2022; Yue et al., 2022).

From the Tuosuo Lake segment of the East Kunlun fault, the large-scale northern boundary of the Bayan Har block progressively bends in a clockwise direction toward the northeastern margin, and the slip rate starts to decrease gradually (Kirby et al., 2007; Ren et al., 2013). With the East Kunlun fault to the north and the Tibet Dagou-Changmahe fault to the south, the area bounded by the two faults forms the Anyemaqen Mountain Restraining Belt (AMRB), in which the mountains were uplifted and the crust was shortening (Li et al., 2011a; Pan et al., 2021). Impeded by the Tibet Dagou-Changmahe fault, it may be difficult for the causative fault of the Maduo earthquake to extend eastward and insert into the AMRB, further making both the source rupture and aftershock sequence terminate at the restraining belt. The AMRB, in turn, probably enhances the strain accumulation in the area where the Maduo earthquake is located, thereby contributing to the occurrence of this event. The significant slips of the Maduo earthquake and the relocated aftershocks are both shallower than 20 km (Fig. 9), suggesting that the seismogenic layer is confined above this depth, and the causative fault cannot extend into the middle and lower crust. This conforms to the viscous tectonic model to some extent, in which a ductile middle-to-lower crust separates the brittle upper crust from the rheologically ductile upper mantle (Royden et al., 1997; Clark and Royden, 2000; Clark et al., 2005; Royden et al., 2008; Li et al., 2021; Zhao et al., 2021b). Because of the topographic gradients and variations in crustal thickness or density, the weak and ductile material in the middle and lower crust that evacuated from the central Tibetan Plateau flow eastward (Clark et al., 2005; Royden et al., 2008; Wang et al., 2008). The tomographic models of Yang et al. (2022) and Zhang et al. (2022a) revealed the anomalies of low seismic velocities and high Poisson's ratio beneath the area hosting the Maduo earthquake, which reflect the existence of crustal fluids. Moreover, the results of the magnetotelluric investigation showed that the upper interface of the high-conductivity/low-resistivity layer beneath the seismogenic fault bends upward, which is consistent with the dome-shaped structure of low velocity anomalies revealed by the tomographic model of Zhang et al. (2022a), implying the seismogenic layer may be weakened by the intrusion of crustal fluids

(Zhan et al., 2021; Yang et al., 2022). Additionally, accompanied by the eastward extrusion of the Tibetan Plateau, the crustal flow beneath the source area of the Maduo earthquake is likely to migrate at a motion rate higher than that of the upper crust (Royden et al., 2008), thereby causing the stress concentration within the upper crust (Zhang et al., 2022a). This will further contribute to the strain accumulation along active faults and triggering earthquakes inside the Bayan Har block (Zheng et al., 2009; Li et al., 2011c; Zhang et al., 2019; Xu et al., 2021). Therefore, we suggest that the tectonic loading in the interior of the block resulted from plate collision, and the eastward extrusion of the Tibetan Plateau involving the weak and ductile material in the middle and lower crust commonly constitute the seismogenic environment of the 2021 Maduo earthquake (Fig. 9).

6. Conclusions

We investigate the source rupture process of the 2021 Maduo earthquake by utilizing the seismological analyses and the joint inversion of seismic and geodetic data. The branch fault model comprises two steeply dipping segments, and the slip distribution demonstrates that the focal mechanism is dominated by the sinistral slip, in which the maximum slip is 4.2 m. The entire source process represents a bilateral rupture pattern and lasts approximately 40 s, releasing a seismic moment of 1.75×10^{20} Nm (M_w 7.43). The spatiotemporal evolution of CFS changes on the fault plane shows that there are interactions of stress triggering between the asperities in the slip distribution, suggesting that the source rupture process of the Maduo earthquake can be attributed to the cascade model. The CFS on the subsidiary faults is significantly increased by the Maduo earthquake, especially the Maduo-Gande and Tibet Dagou-Changmahe faults receive the largest stress loading. Since the CFS on the Tuosuo Lake and Maqin-Maqu segments of the East Kunlun fault is also increased, the corresponding seismic hazard may be increased and deserves further attention. In addition, the occurrences of the 1947 Dari and 2021 Maduo earthquakes suggest that the subsidiary faults inside the Bayan Har block can effectively accumulate strain and have the potential to cause large earthquakes, so that the seismic hazard of the internal faults of the block should not be neglected. The slip

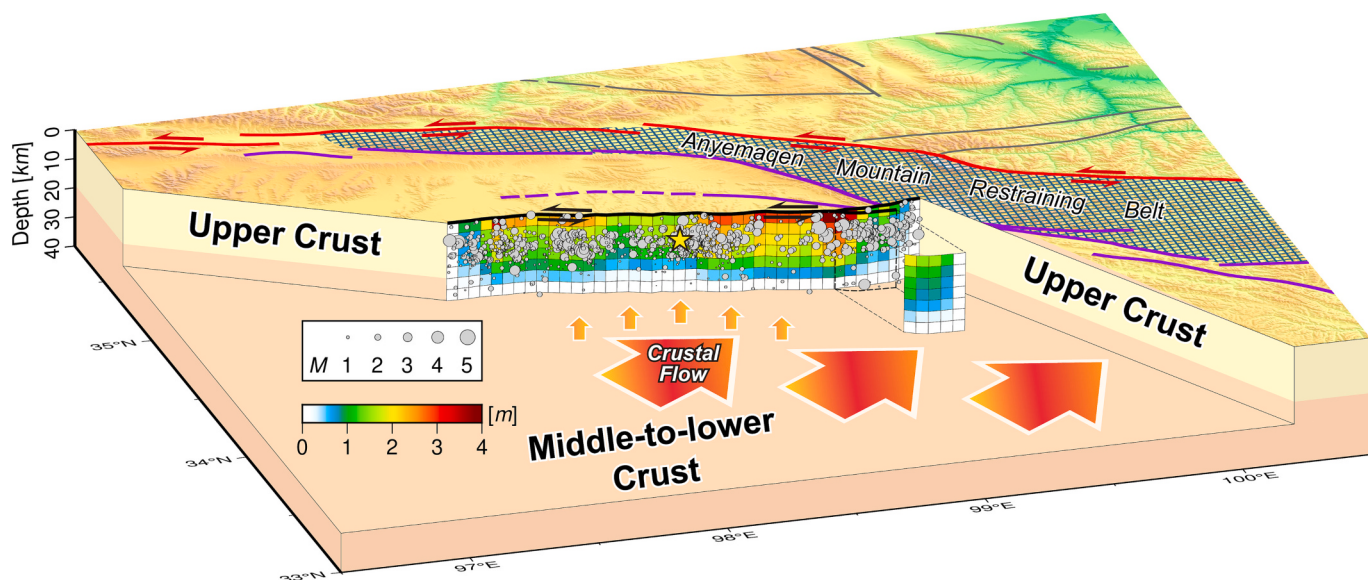


Fig. 9. A conceptual model showing the slip distribution and seismogenesis of the 2021 Maduo earthquake. The significant slips of the mainshock and the relocated aftershocks are confined in the upper crust. The AMRB may obstruct the eastward extension of the earthquake sequence, implying the accumulation of tectonic strain is probably enhanced in the source area on the west of the AMRB. Furthermore, the crustal flow accompanied by the eastward extrusion of the Tibetan Plateau bends upward and migrates at a motion rate higher than that of the upper crust, which is beneficial to accumulate strain in the brittle upper crust. Consequently, we suggest that the internal deformation of the Bayan Har block caused by plate collision and the eastward extrusion of the Tibetan Plateau involving the middle-to-lower crustal flow commonly constitute the seismogenic environment of the 2021 Maduo earthquake.

distribution illustrates that the source rupture is mainly concentrated in the brittle upper crust. The AMRB probably hinders the eastward extension of the earthquake sequence implying the strain accumulation is likely to be enhanced in the source area. We propose that the internal deformation of the Bayan Har block caused by plate collision, together with the eastward extrusion of the Tibetan Plateau involving the middle-to-lower crustal flow commonly constitute the seismogenic environment of the 2021 Maduo earthquake and ultimately lead to the occurrence of this event.

CRediT authorship contribution statement

Ao Zheng: Conceptualization, Methodology, Software, Investigation, Writing – original draft, Funding acquisition. **Xiangwei Yu:** Validation, Data curation, Writing – review & editing. **Jiaqi Qian:** Investigation, Data curation, Writing – review & editing. **Xiaoge Liu:** Validation, Investigation, Data curation. **Wenbo Zhang:** Resources, Writing – review & editing, Supervision, Project administration, Funding acquisition. **Xiaofei Chen:** Supervision, Project administration, Funding acquisition. **Wenbin Xu:** Resources, Data curation, Funding acquisition.

Declaration of Competing Interest

The authors declare that they have no known competing financial interests or personal relationships that could have appeared to influence the work reported in this paper.

Data availability

The teleseismic waveforms are recorded by the International Federation of Digital Seismograph Networks (FDSN), accessed through IRIS DMC (http://ds.iris.edu/wilber3/find_stations/11417068). The strong-motion data are recorded by the China Strong Motion Network and accessed through the Institute of Engineering Mechanics, CEA. All waveform data are processed by ObsPy (Krischer et al., 2015). This work also uses Copernicus data from the Sentinel-1 satellite constellation provided by the European Space Agency (ESA, <http://scihub.copernicus.eu>). Data providers require user registration to gain access, and the granule names are listed in Table S3. The InSAR data processing makes use of the GAMMA software and MATLAB. All processed InSAR and seismic waveform data are publicly available from [http://doi.org/10.5281/zenodo.5587450](https://doi.org/10.5281/zenodo.5587450). The static GPS displacements used in this study are collected from Wang et al. (2021a). The Generic Mapping Tools (GMT) developed by Wessel et al. (2013) is used to plot the figures.

Acknowledgments

The comments from Editor Claire Currie and two anonymous reviewers are helpful in improving the manuscript. This work is supported by the National Key Research and Development Program of China (grant number 2022YFC3003504); the National Natural Science Foundation of China (grant numbers U1901602, 41790465, 42074062 and 42174023); the China Postdoctoral Science Foundation (grant number 2022M720141); and the Fundamental Research Funds for the Central Universities of China (grant number E2E40405).

Appendix A. Supplementary data

Supplementary data to this article can be found online at <https://doi.org/10.1016/j.tecto.2023.229732>.

References

- Bao, H., Ampuero, J.P., Meng, L.S., Fielding, E.J., Liang, C., Milliner, C.W.D., et al., 2019. Early and persistent supershear rupture of the 2018 magnitude 7.5 Palu earthquake. *Nat. Geosci.* 12 (3), 200–205. <https://doi.org/10.1038/s41561-018-0297-z>.
- Beroza, G.C., Ellsworth, W.L., 1996. Properties of the seismic nucleation phase. *Tectonophysics* 261 (1–3), 209–227. [https://doi.org/10.1016/0040-1951\(96\)00067-4](https://doi.org/10.1016/0040-1951(96)00067-4).
- Bouchon, M., Durand, V., Marsan, D., Karabulut, H., Schmittbuhl, J., 2013. The long precursory phase of most large interplate earthquakes. *Nat. Geosci.* 6 (4), 299–302. <https://doi.org/10.1038/ngeo1770>.
- Brocher, T.A., 2005. Empirical relations between elastic wavespeeds and density in the earth's crust. *Bull. Seismol. Soc. Am.* 95 (6), 2081–2092. <https://doi.org/10.1785/01200500077>.
- Chen, C.W., Zebker, H.A., 2001. Two-dimensional phase unwrapping with use of statistical models for cost functions in nonlinear optimization. *J. Opt. Soc. Am. A* 18 (2), 338–351. <https://doi.org/10.1364/josaa.18.000338>.
- Chen, K.J., Xu, W.B., Mai, P.M., Gao, H., Zhang, L., Ding, X.L., 2018. The 2017 Mw 7.3 Sarpol Zahab earthquake, Iran: a compact blind shallow-dipping thrust event in the mountain front fault basement. *Tectonophysics* 747, 108–114. <https://doi.org/10.1016/j.tecto.2018.09.015>.
- Chen, H., Qu, C.Y., Zhao, D.Z., Ma, C., Shan, X.J., 2021. Rupture Kinematics and Coseismic Slip Model of the 2021 Mw 7.3 Maduo (China) earthquake: Implications for the Seismic Hazard of the Kunlun Fault. *Remote Sens.* 13 (16) <https://doi.org/10.3390/rs13163327>.
- Chen, K.J., Avouac, J.P., Geng, J.H., Liang, C.R., Zhang, Z.G., Li, Z.C., et al., 2022. The 2021 Mw 7.4 Maoji Earthquake: an Archetype Bilateral Slip-Pulse Rupture arrested at a Splay Fault. *Geophys. Res. Lett.* 49 (2), e2021GL095243 <https://doi.org/10.1029/2021gl095243>.
- Clark, M.K., Royden, L.H., 2000. Topographic ooze: building the eastern margin of Tibet by lower crustal flow. *Geology* 28 (8), 703–706. [https://doi.org/10.1130/0091-7613\(2000\)28<703:Tobtem>2.0.Co;2](https://doi.org/10.1130/0091-7613(2000)28<703:Tobtem>2.0.Co;2).
- Clark, M.K., Bush, J.W.M., Royden, L.H., 2005. Dynamic topography produced by lower crustal flow against rheological strength heterogeneities bordering the Tibetan Plateau. *Geophys. J. Int.* 162 (2), 575–590. <https://doi.org/10.1111/j.1365-246X.2005.02580.x>.
- Deng, Q.D., Zhang, P.Z., Ran, Y.K., Yang, X.P., Min, W., Chu, Q.Z., 2003. Basic characteristics of active tectonics of China. *Sci. China Ser. D Earth Sci.* 46 (4), 356–372.
- Duputel, Z., Rivera, L., Kanamori, H., Hayes, G., 2012. W phase source inversion for moderate to large earthquakes (1990–2010). *Geophys. J. Int.* 189 (2), 1125–1147. <https://doi.org/10.1111/j.1365-246X.2012.05419.x>.
- Dziewonski, A.M., Anderson, D.L., 1981. Preliminary Reference Earth Model. *Phys. Earth Planet. Inter.* 25 (4), 297–356. [https://doi.org/10.1016/0031-9201\(81\)90046-7](https://doi.org/10.1016/0031-9201(81)90046-7).
- Ekstrom, G., Nettles, M., Dziewonski, A.M., 2012. The global CMT project 2004–2010: Centroid-moment tensors for 13,017 earthquakes. *Phys. Earth Planet. Inter.* 200, 1–9. <https://doi.org/10.1016/j.pepi.2012.04.002>.
- Ellsworth, W.L., Beroza, G.C., 1995. Seismic evidence for an earthquake nucleation phase. *Science* 268 (5212), 851–855. <https://doi.org/10.1126/science.268.5212.851>.
- Ellsworth, W.L., Bulut, F., 2018. Nucleation of the 1999 Izmit earthquake by a triggered cascade of foreshocks. *Nat. Geosci.* 11 (7), 531–535. <https://doi.org/10.1038/s41561-018-0145-1>.
- Farr, T.G., Rosen, P.A., Caro, E., Crippen, R., Duren, R., Hensley, S., et al., 2007. The shuttle radar topography mission. *Rev. Geophys.* 45 (2) <https://doi.org/10.1029/2005rg000183>.
- Freed, A.M., 2005. Earthquake triggering by static, dynamic, and postseismic stress transfer. *Annu. Rev. Earth Planet. Sci.* 33, 335–367. <https://doi.org/10.1146/annurev.earth.33.092203.122505>.
- Gomberg, J., 2018. Unsettled earthquake nucleation. *Nat. Geosci.* 11 (7), 463–464. <https://doi.org/10.1038/s41561-018-0149-x>.
- Guo, J.M., Lin, A.M., Sun, G.Q., Zheng, J.J., 2007. Surface ruptures associated with the 1937 M 7.5 Tuosu Lake and the 1963 M 7.0 Alake Lake earthquakes and the paleoseismicity along the Tuosu Lake segment of the Kunlun fault, northern Tibet. *Bull. Seismol. Soc. Am.* 97 (2), 474–496. <https://doi.org/10.1785/0120050103>.
- Guo, R.M., Yang, H.F., Li, Y., Zheng, Y., Zhang, L.P., 2022. Complex Slip distribution of the 2021 Mw 7.4 Maduo, China, earthquake: an Event Occurring on the Slowly Slipping Fault. *Seismol. Res. Lett.* 93 (2A), 653–665. <https://doi.org/10.1785/0220210226>.
- Hardebeck, J.L., Nazareth, J.J., Hauksson, E., 1998. The static stress change triggering model: Constraints from two southern California aftershock sequences. *J. Geophys. Res. Solid Earth* 103 (B10), 24427–24437. <https://doi.org/10.1029/98jb00573>.
- Hartzell, S.H., Heaton, T.H., 1983. Inversion of strong ground motion and teleseismic waveform data for the fault rupture history of the 1979 Imperial Valley, California, earthquake. *Bull. Seismol. Soc. Am.* 73 (6), 1553–1583.
- Hayes, G.P., Rivera, L., Kanamori, H., 2009. Source Inversion of the W-Phase: Real-time Implementation and Extension to Low Magnitudes. *Seismol. Res. Lett.* 80 (5), 817–822. <https://doi.org/10.1785/gssrl.80.5.817>.
- He, L.J., Feng, G.C., Wu, X.X., Lu, H., Xu, W.B., Wang, Y.D., et al., 2021. Coseismic and early Postseismic Slip Models of the 2021 Mw 7.4 Maduo Earthquake (Western China) estimated by Space-based Geodetic Data. *Geophys. Res. Lett.* 48 (24), e2021GL095860 <https://doi.org/10.1029/2021gl095860>.
- He, K.F., Wen, Y.M., Xu, C.J., Zhao, Y.W., 2022. Fault Geometry and Slip distribution of the 2021 Mw 7.4 Maduo, China, Earthquake Inferred from InSAR Measurements and Relocated aftershocks. *Seismol. Res. Lett.* 93 (1), 8–20. <https://doi.org/10.1785/0220210204>.

- Hong, S., Liu, M., Liu, T., Dong, Y., Chen, L., Meng, G., et al., 2022. Fault Source Model and stress changes of the 2021 Mw 7.4 Maduo Earthquake, China, Constrained by InSAR and GPS Measurements. *Bull. Seismol. Soc. Am.* 112 (3), 1284–1296. <https://doi.org/10.1785/0120210250>.
- Huang, H., Meng, L.S., Burgmann, R., Wang, W., Wang, K., 2020. Spatio-temporal foreshock evolution of the 2019 M 6.4 and M 7.1 Ridgecrest, California earthquakes. *Earth Planet. Sci. Lett.* 551, 116582. <https://doi.org/10.1016/j.epsl.2020.116582>.
- Ishii, M., Shearer, P.M., Houston, H., Vidale, J.E., 2005. Extent, duration and speed of the 2004 Sumatra-Andaman earthquake imaged by the Hi-net array. *Nature* 435 (7044), 933–936. <https://doi.org/10.1038/nature03675>.
- Jian, H.Z., Gong, W.Y., Li, Y.C., Wang, L.F., 2022. Bayesian Inference of Fault Slip and Coupling along the Tuosuo Lake Segment of the Kunlun Fault, China. *Geophys. Res. Lett.* 49 (7), e2021GL096882. <https://doi.org/10.1029/2021gl096882>.
- Jiang, Z.S., Wang, M., Wang, Y.Z., Wu, Y.Q., Che, S., Shen, Z.K., et al., 2014. GPS constrained coseismic source and slip distribution of the 2013 Mw6.6 Lushan, China, earthquake and its tectonic implications. *Geophys. Res. Lett.* 41 (2), 407–413. <https://doi.org/10.1029/2013gl058812>.
- Jin, Z.Y., Fialko, Y., 2021. Coseismic and early Postseismic Deformation due to the 2021 M7.4 Maduo (China) Earthquake. *Geophys. Res. Lett.* 48 (21), e2021GL095213. <https://doi.org/10.1029/2021gl095213>.
- Jónsson, S., Zebker, H., Segall, P., Amelung, F., 2002. Fault slip distribution of the 1999 Mw 7.1 Hector Mine, California, earthquake, estimated from satellite radar and GPS measurements. *Bull. Seismol. Soc. Am.* 92 (4), 1377–1389. <https://doi.org/10.1785/0120000922>.
- Kanamori, H., Rivera, L., 2008. Source inversion of W phase: speeding up seismic tsunami warning. *Geophys. J. Int.* 175 (1), 222–238. <https://doi.org/10.1111/j.1365-246X.2008.03887.x>.
- Kato, A., Ben-Zion, Y., 2021. The generation of large earthquakes. *Nat. Rev. Earth Environ.* 2 (1), 26–39. <https://doi.org/10.1038/s43017-020-00108-w>.
- Kato, A., Obara, K., Igarashi, T., Tsuruoka, H., Nakagawa, S., Hirata, N., 2012. Propagation of Slow Slip Leading up to the 2011 Mw 9.0 Tohoku-Oki Earthquake. *Science* 335 (6069), 705–708. <https://doi.org/10.1126/science.1215141>.
- King, G.C.P., Stein, R.S., Lin, J., 1994. Static stress changes and the triggering of earthquakes. *Bull. Seismol. Soc. Am.* 84 (3), 935–953. <https://doi.org/10.1785/BSSA0840030935>.
- Kirby, E., Harkins, N., Wang, E.Q., Shi, X.H., Fan, C., Burbank, D., 2007. Slip rate gradients along the eastern Kunlun fault. *Tectonics* 26 (2), TC2010. <https://doi.org/10.1029/2006tc002033>.
- Kiser, E., Ishii, M., 2017. Back-Projection Imaging of Earthquakes. *Annu. Rev. Earth Planet. Sci.* 45, 271–299. <https://doi.org/10.1146/annurev-earth-063016-015801>.
- Krischer, L., Megies, T., Barsch, R., Beyreuther, M., Lecocq, T., Caudron, C., et al., 2015. ObsPy: a bridge for seismology into the scientific Python ecosystem. *Comput. Sci. Discov.* 8 (1), 014003. <https://doi.org/10.1088/1749-4699/8/1/014003>.
- Kruger, F., Ohrnberger, M., 2005. Tracking the rupture of the Mw=9.3 Sumatra earthquake over 1,150 km at teleseismic distance. *Nature* 435 (7044), 937–939. <https://doi.org/10.1038/nature03696>.
- Laske, G., Masters, G., Ma, Z., Pasyanos, M., 2013. Update on CRUST1.0 - A 1-degree global model of Earth's crust. Paper presented at the 2013 EGU General Assembly, Vienna, Austria.
- Li, Z.W., Ding, X., Huang, C., Zhu, J.J., Chen, Y.L., 2008. Improved filtering parameter determination for the Goldstein radar interferogram filter. *ISPRS J. Photogramm. Remote Sens.* 63 (6), 621–634. <https://doi.org/10.1016/j.isprsjprs.2008.03.001>.
- Li, C.X., Xu, X.W., Wen, X.Z., Zheng, R.Z., Chen, G.H., Yang, H., et al., 2011a. Rupture segmentation and slip partitioning of the mid-eastern part of the Kunlun Fault, north Tibetan Plateau. *Sci. China-Earth Sci.* 54 (11), 1730–1745. <https://doi.org/10.1007/s11430-011-4239-5>.
- Li, Z.H., Elliott, J.R., Feng, W.P., Jackson, J.A., Parsons, B.E., Walters, R.J., 2011b. The 2010 Mw 6.8 Yushu (Qinghai, China) earthquake: Constraints provided by InSAR and body wave seismology. *J. Geophys. Res. Solid Earth* 116. <https://doi.org/10.1029/2011jb008358>.
- Li, Z.W., Xu, Y., Huang, R.Q., Hao, T.Y., Xu, Y., Liu, J.S., et al., 2011c. Crustal P-wave velocity structure of the Longmenshan region and its tectonic implications for the 2008 Wenchuan earthquake. *Sci. China-Earth Sci.* 54 (9), 1386–1393. <https://doi.org/10.1007/s11430-011-4177-2>.
- Li, Y.Q., Jia, D., Wang, M.M., Shaw, J.H., He, J.K., Lin, A.M., et al., 2014. Structural geometry of the source region for the 2013 Mw 6.6 Lushan earthquake: Implication for earthquake hazard assessment along the Longmen Shan. *Earth Planet. Sci. Lett.* 390, 275–286. <https://doi.org/10.1016/j.epsl.2014.01.018>.
- Li, H.B., Pan, J.W., Lin, A.M., Sun, Z.M., Liu, D.L., Zhang, J.J., et al., 2016. Coseismic Surface Ruptures Associated with the 2014 Mw 6.9 Yutian Earthquake on the Altyn Tagh Fault, Tibetan Plateau. *Bull. Seismol. Soc. Am.* 106 (2), 595–608. <https://doi.org/10.1785/0220150136>.
- Li, X., Xu, W.B., Jonsson, S., Klinger, Y., Zhang, G.H., 2020. Source Model of the 2014 Mw 6.9 Yutian Earthquake at the Southwestern end of the Altyn Tagh Fault in Tibet estimated from Satellite Images. *Seismol. Res. Lett.* 91 (6), 3161–3170. <https://doi.org/10.1785/0220190361>.
- Li, L., Zhang, X.Z., Liao, J., Liang, Y.L., Dong, S.X., 2021. Geophysical constraints on the nature of lithosphere in central and eastern Tibetan plateau. *Tectonophysics* 804. <https://doi.org/10.1016/j.tecto.2021.228722>.
- Li, Q., Wan, Y.G., Li, C.T., Tang, H., Tan, K., Wang, D.Z., 2022. Source Process Featuring Asymmetric Rupture Velocities of the 2021 Mw 7.4 Maduo, China, earthquake from Teleseismic and Geodetic Data. *Seismol. Res. Lett.* 93 (3), 1429–1439. <https://doi.org/10.1785/0220210300>.
- Lindh, A.G., Boore, D.M., 1981. Control of Rupture by Fault Geometry during the 1966 Parkfield Earthquake. *Bull. Seismol. Soc. Am.* 71 (1), 95–116.
- Liu, J.H., Hu, J., Li, Z.W., Ma, Z.F., Wu, L.X., Jiang, W.P., et al., 2022. Complete three-dimensional coseismic displacements due to the 2021 Maduo earthquake in Qinghai Province, China from Sentinel-1 and ALOS-2 SAR images. *Sci. China-Earth Sci.* 65 (4), 687–697. <https://doi.org/10.1007/s11430-021-9868-9>.
- Lyu, M., Chen, K., Xue, C., Zang, N., Zhang, W., Wei, G., 2022. Overall subshear but locally supershear rupture of the 2021 Mw 7.4 Maduo earthquake from high-rate GNSS waveforms and three-dimensional InSAR deformation. *Tectonophysics* 839, 229542. <https://doi.org/10.1016/j.tecto.2022.229542>.
- Marsan, D., Lengline, O., 2008. Extending earthquakes' reach through cascading. *Science* 319 (5866), 1076–1079. <https://doi.org/10.1126/science.1148783>.
- Melgar, D., Bock, Y., 2015. Kinematic earthquake source inversion and tsunami runup prediction with regional geophysical data. *J. Geophys. Res. Solid Earth* 120 (5), 3324–3349. <https://doi.org/10.1002/2014jb011832>.
- Meng, L.S., Inbal, A., Ampuero, J.P., 2011. A window into the complexity of the dynamic rupture of the 2011 Mw 9 Tohoku-Oki earthquake. *Geophys. Res. Lett.* 38. <https://doi.org/10.1029/2011gl048118>.
- Molnar, P., Deng, Q.D., 1984. Faulting Associated with large Earthquakes and the Average Rate of Deformation in Central and Eastern Asia. *J. Geophys. Res.* 89 (Nb7), 6203–6227. <https://doi.org/10.1029/JB089IB07p06203>.
- Molnar, P., Tappponnier, P., 1975. Cenozoic Tectonics of Asia: Effects of a Continental Collision. *Science* 189 (4201), 419–426. <https://doi.org/10.1126/science.189.4201.419>.
- Olson, A.H., Apsel, R.J., 1982. Finite faults and inverse-theory with applications to the 1979 Imperial Valley earthquake. *Bull. Seismol. Soc. Am.* 72 (6), 1969–2001.
- Ou, Q., Daoit, S., Weiss, J.R., Shen, L., Lazecý, M., Wright, T.J., et al., 2022. Large-Scale Interseismic Strain Mapping of the NE Tibetan Plateau from Sentinel-1 Interferometry. *J. Geophys. Res. Solid Earth* 127 (6), e2022JB024176. <https://doi.org/10.1029/2022JB024176>.
- Pan, J., Bai, M., Li, C., Liu, F., Li, H., Liu, D., et al., 2021. Coseismic surface rupture and seismogenic structure of the 2021-05-22 Maduo (Qinghai) Ms7.4 earthquake. *Acta Geol. Sin.* 95 (06), 1655–1670. <https://doi.org/10.19762/j.cnki.dizhixuebao.2021116>.
- Qian, Y.Y., Ni, S.D., Wei, S.J., Almeida, R., Zhang, H., 2017. The effects of core-reflected waves on finite fault inversions with teleseismic body wave data. *Geophys. J. Int.* 211 (2), 936–951. <https://doi.org/10.1093/gji/ggx338>.
- Ren, J.J., Xu, X.W., Yeats, R.S., Zhang, S.M., 2013. Millennial slip rates of the Tazang fault, the eastern termination of Kunlun fault: Implications for strain partitioning in eastern Tibet. *Tectonophysics* 608, 1180–1200. <https://doi.org/10.1016/j.tecto.2013.06.026>.
- Ren, J.J., Xu, X.W., Zhang, G.W., Wang, Q.X., Zhang, Z.W., Gai, H.L., et al., 2022. Coseismic surface ruptures, slip distribution, and 3D seismogenic fault for the 2021 Mw 7.3 Maduo earthquake, central Tibetan Plateau, and its tectonic implications. *Tectonophysics* 827, 229275. <https://doi.org/10.1016/j.tecto.2022.229275>.
- Royden, L.H., Burchfiel, B.C., King, R.W., Wang, E., Chen, Z.L., Shen, F., et al., 1997. Surface deformation and lower crustal flow in eastern Tibet. *Science* 276 (5313), 788–790. <https://doi.org/10.1126/science.276.5313.788>.
- Royden, L.H., Burchfiel, B.C., van der Hilst, R.D., 2008. The geological evolution of the Tibetan plateau. *Science* 321 (5892), 1054–1058. <https://doi.org/10.1126/science.1155371>.
- Shan, B., Xiong, X., Wang, R.J., Zheng, Y., Yadav, R.B.S., 2015. Stress evolution and seismic hazard on the Maqin-Maqu segment of East Kunlun Fault zone from co-, post- and interseismic stress changes. *Geophys. J. Int.* 200 (1), 244–253. <https://doi.org/10.1093/gji/gju395>.
- Shen, Z.K., Sun, J.B., Zhang, P.Z., Wan, Y.G., Wang, M., Burgmann, R., et al., 2009. Slip maxima at fault junctions and rupturing of barriers during the 2008 Wenchuan earthquake. *Nat. Geosci.* 2 (10), 718–724. <https://doi.org/10.1038/ngeo636>.
- Shen, W., Ritzwoller, M.H., Kang, D., Kim, Y.H., Lin, F.C., Ning, J., et al., 2016. A seismic reference model for the crust and uppermost mantle beneath China from surface wave dispersion. *Geophys. J. Int.* 206 (2), 954–979. <https://doi.org/10.1093/gji/ggw175>.
- Stein, R.S., 1999. The role of stress transfer in earthquake occurrence. *Nature* 402 (6762), 605–609. <https://doi.org/10.1038/45144>.
- Stein, R.S., 2003. Earthquake conversations. *Sci. Am.* 288 (1), 72–79. <https://doi.org/10.1038/scientificamerican0103-72>.
- Sun, J.B., Yue, H., Shen, Z.K., Fang, L.H., Zhan, Y., Sun, X.Y., 2018. The 2017 Jiuzhaigou Earthquake: a Complicated Event Occurred in a Young Fault System. *Geophys. Res. Lett.* 45 (5), 2230–2240. <https://doi.org/10.1002/2017gl076421>.
- Tape, C., Holtkamp, S., Silwal, V., Hawthorne, J., Kaneko, Y., Ampuero, J.P., et al., 2018. Earthquake nucleation and fault slip complexity in the lower crust of Central Alaska. *Nat. Geosci.* 11 (7), 536–541. <https://doi.org/10.1038/s41561-018-0144-2>.
- Tappponnier, P., Molnar, P., 1977. Active faulting and tectonics in China. *J. Geophys. Res.* 82 (20), 2905–2930. <https://doi.org/10.1029/JB082i020p02905>.
- Tappponnier, P., Peltzer, G., Ledain, A.Y., Armijo, R., Cobbold, P., 1982. Propagating extrusion tectonics in Asia: New insights from simple experiments with plasticine. *Geology* 10 (12), 611–616. [https://doi.org/10.1130/0091-7613\(1982\)10<611:petian>2.0.co;2](https://doi.org/10.1130/0091-7613(1982)10<611:petian>2.0.co;2).
- Tappponnier, P., Xu, Z.Q., Roger, F., Meyer, B., Arnaud, N., Wittlinger, G., et al., 2001. Geology - Oblique stepwise rise and growth of the Tibet plateau. *Science* 294 (5547), 1671–1677. <https://doi.org/10.1126/science.105978>.
- Toda, S., Stein, R.S., Sevilgen, V., Lin, J., 2011. Coulomb 3.3 graphic-rich deformation and stress-change software for earthquake, tectonic, and volcano research and teaching-user guide. In: U.S. Geological Survey Open-File Report 2011-1060.
- Tong, X.P., Xu, X.H., Chen, S., 2022. Coseismic Slip Model of the 2021 Maduo Earthquake, China from Sentinel-1 InSAR Observation. *Remote Sens.* 14 (3), 436. <https://doi.org/10.3390/rs14030436>.

- Wald, D.J., Heaton, T.H., Hudnut, K.W., 1996. The slip history of the 1994 Northridge, California, earthquake determined from strong-motion, teleseismic, GPS, and leveling data. *Bull. Seismol. Soc. Am.* 86 (1), S49–S70.
- Wang, M., Shen, Z.K., 2020. Present-Day Crustal Deformation of Continental China Derived from GPS and its Tectonic Implications. *J. Geophys. Res. Solid Earth* 125 (2), e2019JB018774. <https://doi.org/10.1029/2019jb018774>.
- Wang, C.Y., Lou, H., Lue, Z.Y., Wu, J.P., Chang, L.J., Dai, S.G., et al., 2008. S-wave crustal and upper mantle's velocity structure in the eastern Tibetan Plateau - deep environment of lower crustal flow. *Sci. China Ser. D Earth Sci.* 51 (2), 263–274. <https://doi.org/10.1007/s11430-008-0008-5>.
- Wang, Q., Qiao, X.J., Lan, Q.Q., Freymueller, J., Yang, S.M., Xu, C.J., et al., 2011. Rupture of deep faults in the 2008 Wenchuan earthquake and uplift of the Longmen Shan. *Nat. Geosci.* 4 (9), 634–640. <https://doi.org/10.1038/ngeo1210>.
- Wang, M., Wang, F., Jiang, X., Tian, J.B., Li, Y., Sun, J.B., et al., 2021a. GPS determined coseismic slip of the 2021 Mw 7.4 Maduo, China, earthquake and its tectonic implication. *Geophys. J. Int.* 228 (3), 2048–2055. <https://doi.org/10.1093/gji/gjab460>.
- Wang, W.L., Fang, L.H., Wu, J.P., Tu, H.W., Chen, L.Y., Lai, G.J., et al., 2021b. Aftershock sequence relocation of the 2021 Ms 7.4 Maduo Earthquake, Qinghai, China. *Sci. China-Earth Sci.* 64 (8), 1371–1380. <https://doi.org/10.1007/s11430-021-9803-3>.
- Wang, S., Song, C., Li, S., Li, X., 2022. Resolving co- and early post-seismic slip variations of the 2021 Mw 7.4 Maduo earthquake in east Bayan Har block with a block-wide distributed deformation mode from satellite synthetic aperture radar data. *Earth Planet. Phys.* 6 (1), 108–122. <https://doi.org/10.26464/epp2022007>.
- Wegmüller, U., Werner, C., Strozzi, T., Wiesmann, A., Frey, O., Santoro, M., 2016. Sentinel-1 support in the GAMMA Software. *Procedia Computer Sci.* 100, 1305–1312. <https://doi.org/10.1016/j.procs.2016.09.246>.
- Wen, X.Z., Yi, G.X., Xu, X.W., 2007. Background and precursory seismicities along and surrounding the Kunlun fault before the M(s)8.1, 2001, Kokoxili earthquake, China. *J. Asian Earth Sci.* 30 (1), 63–72. <https://doi.org/10.1016/j.jseas.2006.07.008>.
- Wessel, P., Smith, W.H.F., Scharroo, R., Luis, J., Wobbe, F., 2013. Generic Mapping Tools: improved Version Released. *EOS Trans. Am. Geophys. Union* 94 (45), 409–410. <https://doi.org/10.1002/2013EO450001>.
- Xu, W., Jónsson, S., Ruch, J., Aoki, Y., 2016. The 2015 Wolf volcano (Galapagos) eruption studied using Sentinel-1 and ALOS-2 data. *Geophys. Res. Lett.* 43 (18), 9573–9580. <https://doi.org/10.1002/2016gl069820>.
- Xu, Z., Liang, S., Zhang, G., Liang, J., Zou, L., Li, X., et al., 2021. Analysis of seismogenic structure of Maduo, Qinghai MS7.4 earthquake on May 22, 2021. *Chin. J. Geophys. Chin. Edition* 64 (08), 2657–2670. <https://doi.org/10.6038/cjg2021P0390>.
- Yang, Z.Q., Zhao, D.P., Dong, Y.P., Cheng, B., 2022. Crustal flow and fluids affected the 2021 M7.4 Maduo earthquake in Northeast Tibet. *J. Asian Earth Sci.* 225, 105050. <https://doi.org/10.1016/j.jseas.2021.105050>.
- Yao, H.J., Shearer, P.M., Gerstoft, P., 2012. Subevent location and rupture imaging using iterative backprojection for the 2011 Tohoku Mw 9.0 earthquake. *Geophys. J. Int.* 190 (2), 1152–1168. <https://doi.org/10.1111/j.1365-246X.2012.05541.x>.
- Yuan, Z., Li, T., Su, P., Sun, H., Ha, G., Guo, P., et al., 2022. Large Surface-Rupture Gaps and Low Surface Fault Slip of the 2021 Mw 7.4 Maduo Earthquake along a Low-activity Strike-Slip Fault, Tibetan Plateau. *Geophys. Res. Lett.* 49 (6), e2021GL096874. <https://doi.org/10.1029/2021GL096874>.
- Yue, H., Shen, Z.-K., Zhao, Z., Wang, T., Cao, B., Li, Z., et al., 2022. Rupture process of the 2021 M7.4 Maduo earthquake and implication for deformation mode of the Songpan-Ganzi terrane in Tibetan Plateau. *Proc. Natl. Acad. Sci.* 119 (23), e2116445119. <https://doi.org/10.1073/pnas.2116445119>.
- Zhan, Y., Liang, M., Sun, X., Huang, F., Zhao, L., Gong, Y., et al., 2021. Deep structure and seismogenic pattern of the 2021.5.22 Maduo (Qinghai) Ms7.4 earthquake. *Chin. J. Geophys. Chin. Edition* 64 (07), 2232–2252. <https://doi.org/10.6038/cjg202100521>.
- Zhang, Y., Xu, L.S., Chen, Y.T., 2010. Source process of the 2010 Yushu, Qinghai, earthquake. *Sci. China-Earth Sci.* 53 (9), 1249–1251. <https://doi.org/10.1007/s11430-010-4045-5>.
- Zhang, G.W., Lei, J.S., Sun, D.Y., 2019. The 2013 and 2017 Ms 5 Seismic Swarms in Jilin, NEChina: Fluid-Triggered Earthquakes? *J. Geophys. Res. Solid Earth* 124 (12), 13096–13111. <https://doi.org/10.1029/2019jb018649>.
- Zhang, X., Feng, W.P., Du, H.L., Li, L., Wang, S., Yi, L., et al., 2020. The 2018 Mw 7.5 Papua New Guinea Earthquake: a Dissipative and Cascading Rupture Process. *Geophys. Res. Lett.* 47 (17), e2020GL089271. <https://doi.org/10.1029/2020gl089271>.
- Zhang, G.W., Li, Y.J., Hu, X.P., 2022a. Nucleation mechanism of the 2021 Mw 7.4 Maduo earthquake, NE Tibetan Plateau: Insights from seismic tomography and numerical modeling. *Tectonophysics* 839, 229528. <https://doi.org/10.1016/j.tecto.2022.229528>.
- Zhang, X., Feng, W.P., Du, H.L., Samsonov, S., Yi, L., 2022b. Supershear Rupture during the 2021 Mw 7.4 Maduo, China, Earthquake. *Geophys. Res. Lett.* 49 (6), e2022GL097984. <https://doi.org/10.1029/2022gl097984>.
- Zhao, D., Qu, C., Chen, H., Shan, X., Song, X., Gong, W., 2021a. Tectonic and Geometric Control on Fault Kinematics of the 2021 Mw7.3 Maduo (China) Earthquake Inferred from Interseismic, Coseismic, and Postseismic InSAR Observations. *Geophys. Res. Lett.* 48 (18), e2021GL095417. <https://doi.org/10.1029/2021GL095417>.
- Zhao, P.P., Chen, J.H., Li, Y., Liu, Q.Y., Chen, Y.F., Guo, B.A., et al., 2021b. Growth of the Northeastern Tibetan Plateau Driven by Crustal Channel Flow: evidence from High-Resolution Ambient Noise Imaging. *Geophys. Res. Lett.* 48 (13), 2021GL093387. <https://doi.org/10.1029/2021GL093387>.
- Zheng, Y., Ma, H.S., Lu, J., Ni, S.D., Li, Y.C., Wei, S.J., 2009. Source mechanism of strong aftershocks ($M \geq 5.6$) of the 2008/05/12 Wenchuan earthquake and the implication for seismotectonics. *Sci. China Ser. D Earth Sci.* 52 (6), 739–753. <https://doi.org/10.1007/s11430-009-0074-3>.
- Zheng, A., Wang, M., Yu, X., Zhang, W., 2018. Source rupture process of the 2016 Kaikoura, New Zealand earthquake estimated from the kinematic waveform inversion of strong-motion data. *Geophys. J. Int.* 212 (3), 1736–1746. <https://doi.org/10.1093/gji/ggx505>.
- Zheng, A., Yu, X., Xu, W., Chen, X., Zhang, W., 2020. A hybrid source mechanism of the 2017 Mw 6.5 Jiuzhaigou earthquake revealed by the joint inversion of strong-motion, teleseismic and InSAR data. *Tectonophysics* 789, 228538. <https://doi.org/10.1016/j.tecto.2020.228538>.
- Zhu, L., Rivera, L.A., 2002. A note on the dynamic and static displacements from a point source in multilayered media. *Geophys. J. Int.* 148 (3), 619–627. <https://doi.org/10.1046/j.1365-246X.2002.01610.x>.
- Zhu, Y.G., Diao, F.Q., Fu, Y.C., Liu, C.L., Xiong, X., 2021. Slip rate of the seismogenic fault of the 2021 Maduo earthquake in western China inferred from GPS observations. *Sci. China-Earth Sci.* 64 (8), 1363–1370. <https://doi.org/10.1007/s11430-021-9808-0>.